REPORT

Microtubule-driven cell shape changes and actomyosin flow synergize to position the centrosome

Alexandre Schaeffer[2] ⓘ, Simona Buracco[1] ⓘ, Morgan Gazzola[2] ⓘ, Matthieu Gelin[2], Benoit Vianay[1] ⓘ, Chiara de Pascalis[2] ⓘ, Laurent Blanchoin[1,2] ⓘ, and Manuel Théry[1,2] ⓘ

The regulation of centrosome position is critical to the alignment of intracellular structures with extracellular cues. The exact nature and spatial distribution of the mechanical forces that bala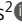nce at the centrosome are unknown. Here, we used laser-based nanoablations in adherent cells and found that forces along microtubules were damped by their anchoring to the actin network, rendering them ineffective in moving the microtubule aster. In contrast, the actomyosin contractile network was responsible for the generation of a centripetal flow that robustly drives the centrosome toward the geometrical center of the cell, even in the absence of microtubules. Unexpectedly, we discovered that the remodeling of cell shape around the centrosome was instrumental in aster centering. The radial array of microtubules and cytoplasmic dyneins appeared to direct this reorganization. This revised view of the respective roles of actin and microtubules in centrosome positioning offers a new perspective for understanding the establishment of cell polarity.

Introduction

The microtubule network is the structural scaffold that supports intracellular organization. Since microtubules serve as tracks for molecular motors, the architecture of the network directs intracellular trafficking, determines the position of organelles, and thus defines the cell body plan (Bornens, 2008). In proliferating cells, the centrosome is the main microtubule-organizing center. By nucleating and anchoring microtubules, it organizes the network into a polarized radial array, with microtubule minus-ends in and plus-ends out (Martin and Akhmanova, 2018). This radial array, which spans the entire cytoplasm, collects, integrates, processes, and redistributes information and resources coming from peripheral sensors and intracellular organelles (Arquint et al., 2014). The position of the center of this array is therefore critical for the adaptation of cell functions to extracellular signals (Tang and Marshall, 2012; Hannaford and Rusan, 2024).

Observing the centrosome in early sea urchin and *Ascaris* embryos, Theodore Bovery named it for its position at the geometrical center of the cell's soma (Scheer, 2014). The name stuck because this remarkable geometric property was quite robust and could be easily observed in most adherent cells in culture.

However, the mechanism ensuring this central positioning remains unclear as numerous studies carried out in different organisms and cell types have generated distinct and apparently contradictory results, particularly with regard to the origin and orientation of the mechanical forces acting on the centrosome (Burakov and Nadezhdina, 2020).

The processes behind centrosome centering have been best characterized in eggs and early embryos (Haupt and Minc, 2018). The large size of these cells enabled direct manipulations and precise mapping of the mechanical forces acting along the microtubule network. Centering appeared to rely on both pushing forces produced by the polymerization of microtubules (Garzon-Coral et al., 2016; Sulerud et al., 2020; Meaders et al., 2020; De-Carvalho et al., 2024) and pulling forces generated by dyneins as they walked toward microtubule minus-ends (Grill et al., 2003; Tanimoto et al., 2016; Farhadifar et al., 2020; Wu et al., 2024). Both mechanisms can ensure a robust centering of the centrosome (Kimura and Kimura, 2011; Grill and Hyman, 2005; Pécréaux et al., 2016; Letort et al., 2016). On the other hand, flows generated by contractions inside the actomyosin network can also direct aster positioning (Field and Lénárt, 2011;

Chaigne et al., 2016; Colin et al., 2020). In mouse oocytes, the actin network autonomously regulates spindle positioning and is responsible for the relocalization of the meiotic spindle at the periphery of the cell (Schuh and Ellenberg, 2008; Azoury et al., 2008; Chaigne et al., 2013). Recent experiments conducted in *Xenopus* egg extracts showing large-scale coordinated motions of microtubule asters, organelles, and actin suggested that they could be seen as a physically integrated gel (Pelletier et al., 2020; Xie et al., 2022). The mechanism underlying the centering of a microtubule aster in such an active and integrated gel remains unclear.

In somatic cells, and particularly in cultured adherent cells, the positioning mechanism remains even more elusive than in eggs and early embryos. Physical forces have not been directly assessed and the parameters involved in centering have been inferred from the cell's response to biochemical changes or geometric constraints. Seminal experiments of dynein inactivation in *Dictyostelium* suggested that dynein pulling forces could be responsible for centrosome centering inside adherent cells (Fig. 1 Ai and ii) (Koonce et al., 1999). However, in mammalian adherent cells, centrosome position was only mildly affected by dynein inactivation or microtubule disassembly (Burakov et al., 2003; Wu et al., 2011; Hale et al., 2011). In addition, and contrary to the radial arrangement of straight microtubules in eggs, the irregular organizations of microtubules and their tortuous shapes inside somatic adherent cells seem incompatible with most models based on either pushing or pulling forces along them (Zhu et al., 2010; Letort et al., 2016). All of this could be partially accounted for by the additional contribution of the actin network, which has been proposed to bind, push and deform microtubules (Burakov et al., 2003; Hale et al., 2011; Brangwynne et al., 2006, 2007, 2008). Indeed our recent work suggested that aster positioning results from the contributions of the actin network, putting it under pressure along the cell periphery, and dyneins putting it under tension closer to the center (Jimenez et al., 2021). Yet, as in eggs and embryos, the attachment of microtubules to the network of actin filaments (Orii and Tanimoto, 2025) questions the possibility of transmitting and integrating forces throughout the microtubule aster. Overall, the origin and spatial distributions of mechanical forces acting on the centrosome in somatic cells remain unclear and require further investigation. Additionally, centrosome localization is a dynamic process, as evidenced by its inducible and transient recruitment to the periphery of the cell in specific contexts such as ciliogenesis or immune synapse formation (Tang and Marshall, 2012; Hooikaas et al., 2020; Meiring et al., 2020). Hence, the mechanism to elucidate should be both robust to ensure reliable centering and flexible to allow decentering of the centrosome (Burakov and Nadezhdina, 2020).

Results and discussion

To assess the exact contributions of microtubule pushing and pulling forces in defining the position of the centrosome, we ablated microtubules using a pulsed laser akin to what had been previously done in eggs and early embryos (Haupt and Minc, 2018) (Fig. 1 A). To reliably visualize the microtubule network,

we worked with PtK2 cells stably expressing GFP-tubulin (Khodjakov et al., 2003). Surprisingly, the ablation of a few microtubules near the centrosome had no significant impact on the centrosome position (Fig. S1 A and Video 1). Considering that the attachment of the centrosome to the nucleus might buffer small variations in the forces acting upon it (Salpingidou et al., 2007; Lombardi et al., 2011), we repeated the experiment in cytoplasts, i.e., enucleated cells, and observed no additional effect (Fig. S1 B and Video 2). To challenge the model of centering based on the balance of mechanical forces, we then ablated approximately half of the microtubules reaching the centrosome. Since the loss of dynamic microtubules can be rapidly compensated by the growth of new ones, we continuously ablated the microtubules reappearing in the ablated region over the following few minutes. However, this harsh surgery resulted in only a barely visible slow recoil (less than half a micron in 3–5 min) of the centrosome away from the ablated region (Fig. 1 B; Fig. S1, C and D; and Video 3). We wondered whether this absence of network relaxation might result from the specific shape and intracellular organization of PtK2 cells. We, therefore, repeated the experiment in other cell types with clearly distinct cytoskeletal architectures: RPE1 cells with smaller sizes and denser microtubule arrays, MEF cells with more irregular shapes, and fewer microtubules (Fig. S1 E). In cytoplasts from both cell types, centrosome recoil after microtubule ablation was as minimal and slow as in PtK2 cells (Fig. S1 F), and markedly different from the 5-µm displacement in about 20 s that had been observed following microtubule ablation in early *Caenorhabditis elegans* embryos (Farhadifar et al., 2020; Wu et al., 2024). Importantly, in all cell types, and in the few cases of clear centrosome recoil, a similar relaxation was also visible in the surrounding actin network (Fig. 1 C; and Fig. S1, G and H). This co-relaxation, induced by the non-specific ablation of actin by pulsed UV laser, suggested that the two networks were connected to each other. Indeed, recent experiments using magnetic tweezers inside adherent cells to displace microtubule asters showed that microtubules and actin form an interacting continuum (Orii and Tanimoto, 2025).

We further investigated the consequences of the entanglement between the two networks by studying the effect of small-scale ablations of individual microtubules. We microinjected low amount of labeled tubulin and actin to generate speckles along both networks, enabling precise monitoring of filament displacements (Salmon et al., 2002). The tubulin speckles allowed us to distinguish microtubule polymerization, depolymerization, or pause from translocation events (Fig. S2 A and Video 4). Similarly, actin speckles revealed filament translocation along stress fibers and fiber displacements (Fig. S2 B and Video 5). Cells were plated on adhesive micropatterns to normalize the architecture of the actin network. We used geometries where cells could spread over non-adhesive regions to induce the formation of contractile bundles that would relax more freely (Vignaud et al., 2021) (Fig. 1 D and Fig. S2 C). The recoil of actin bundles and microtubules was measured by tracking the displacement of individual speckles (Fig. S2 D). Local ablations led to either microtubule disassembly with no detectable effect on actin bundles, or to the recoil of both microtubules and actin
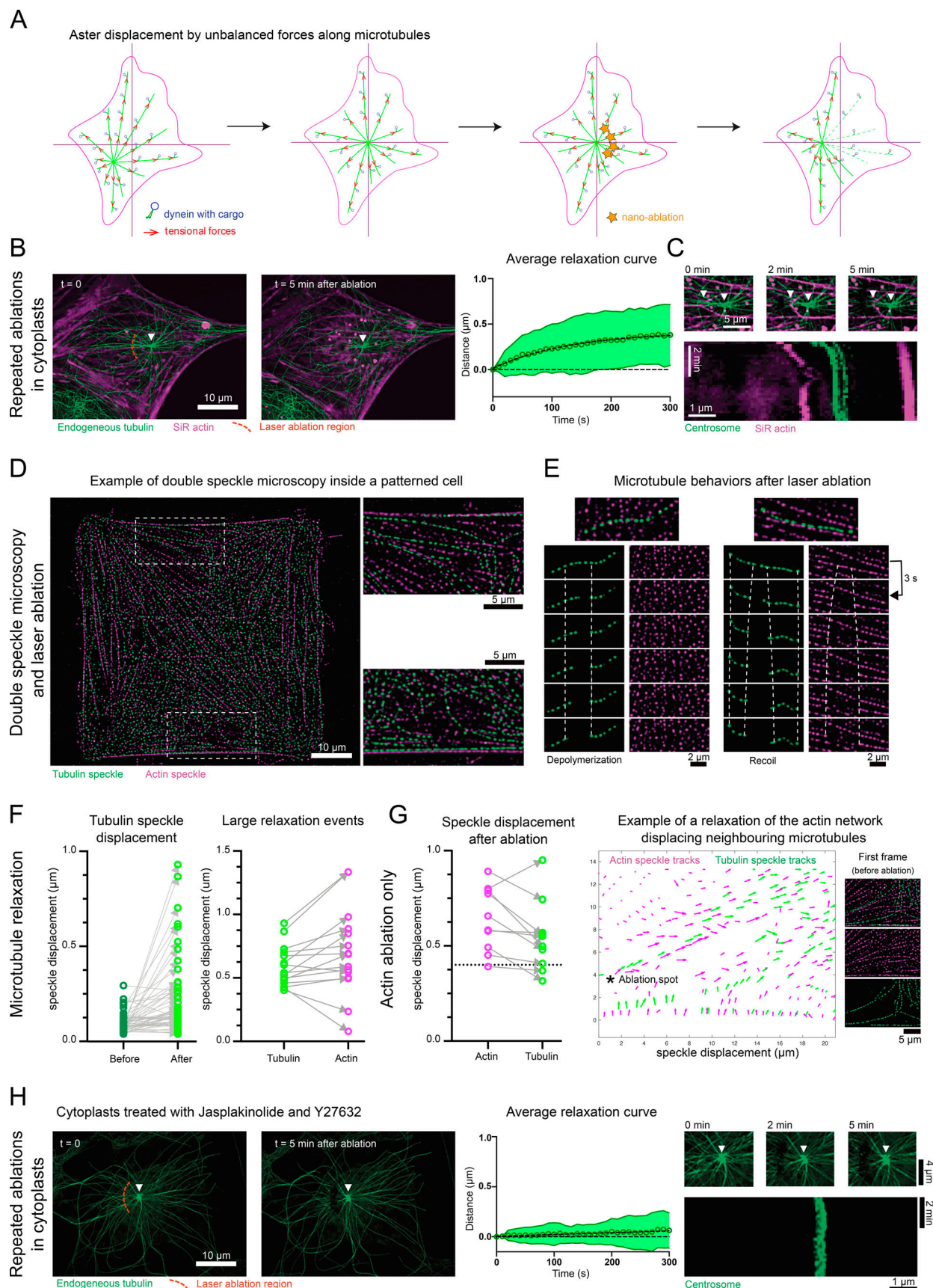
Figure 1. **Aster relaxation upon microtubule ablation. (A)** Schematic representation of dynein-generated tensional stresses along microtubules leading to centrosome centration and centrosome maintenance at the center of the cell when a mechanical force balance is reached. In this context, ablating microtubules

on one side of the centrosome will lead to a disruption of the mechanical force balance and recoil of the centrosomal aster away from the ablated area in the direction of the remaining net pulling force. **(B)** On the left, first, and last time points of a laser ablation experiment in a cytoplast from a PtK2 cells expressing GFP-tubulin. Actin was stained using SiR actin. Images are max projections, further processed using an unsharp mask, a gamma filter, and a subtract background function. Microtubules were repeatedly ablated on one side of the centrosome for 5 min. The white triangular marks indicate the position of the centrosome. On the right, the graph representing the average relaxation curve shows the mean relaxation profile of the centrosomes (n = 22) during the 5 min laser ablation experiment. The displacement of the centrosome was projected along an axis connecting the centroid of the ablated area and the centrosome (for a graphical representation see Fig. S1 C). The circles represent the average displacement of the centrosome at each time point, the continuous lines represent the standard deviation. **(C)** Zoomed-in view of the centrosomal area of the cytoplast shown in B. White arrows indicate from left to right a recoiling actin structure and the centrosome position. Kymograph representation of the centrosome and actin relaxations inside the zoomed-in area. The kymograph (scaled three times to smoothen the signal) was performed along a straight line connecting the centrosome with the ablated area and spanning the entire length of the zoomed-in area. **(D)** Representative live image of a control PtK2 cell microinjected with both actin and tubulin on a 3,500 μm² H-shaped micropattern. On the right, two magnified regions show actin and tubulin speckles in higher detail. For details regarding actin and tubulin speckle processing, see the dedicated section in the Materials and methods. **(E)** Representative responses of single microtubules in the 15 s that followed laser ablation. Left images show microtubule depolymerization after laser ablation with no mechanical relaxation. Right images show actin stress fiber recoiling after laser ablation accompanied by a local microtubule buckling and recoiling. **(F)** Graphs show the displacements of tubulin speckles before and after ablation (n = 121, left), and the displacements of tubulin and actin speckles after laser ablation in the cases of large relaxation events (displacements >400 nm) (n = 15, right). **(G)** Microtubule displacement events when only actin was ablated. The graph shows the motion of tubulin speckle and actin speckle after ablation. The dotted line marks the 400 nm threshold used to define large relaxation events (n = 10). Vector map depicting the coordinated displacements of actin and tubulin speckles after an actin ablation event (over a 15 s period). Images of the actin and tubulin speckles localization before the laser ablation event. **(H)** Same as B in a PtK2 cytoplast expressing GFP-tubulin treated with Jasplakinolide (600 nm) and Y27632 (20 μM) for 4 h (n = 24).

bundles (Fig. 1 E and Video 6). Most microtubule recoils were <200 nm. The few recoils that were >400 nm were associated with a similar recoil of the local actin network, which was also disrupted during laser ablation (Fig. 1 F and Fig. S2 E). We then sought to ablate solely actin structures localized in close proximity to microtubules to assess the contribution of actin in the previously described co-relaxation events. Specific ablations of actin bundles were consistently associated with microtubule recoils of similar amplitude to those we had previously observed. Importantly, the severing of actin bundles also resulted in the displacement of distant microtubules (Fig. 1 G and Video 7). These experiments therefore confirmed that microtubules were not free in the cytoplasm but rather connected to actin bundles along their length. Interestingly, in conditions where the actin network was "frozen" by blocking actin filament dynamics (with Jasplakinolide) and translocations (with ROCK inhibitor) (Peng et al., 2011), large and repeated ablations of microtubules did not induce any detectable relaxation of the centrosome, despite the removal of more than half of the centrosomal microtubules (Fig. 1 H, Fig. S1 D, and Video 8). These results showed that, in interphasic adherent cells, contrary to previous observations in eggs or embryos, the entanglement of microtubules within the network of actin filaments prevented their tensile or pressure forces from affecting centrosome position.

To further challenge the implication of microtubules in the regulation of centrosome positioning, we disassembled most microtubules by treating cells with Nocodazole. To limit the confounding effect of the associated increase in cellular contractility (Rafiq et al., 2019; Seetharaman et al., 2021), we cotreated the cells with a Rho kinase inhibitor. A low dose of Y27632 (1 μM) was not able to fully compensate for the overcontraction induced by microtubule disassembly. Alternatively, a higher concentration of Y27632 (30 μM) led to the disassembly of most actin contractile structures in cells treated with 6 μM of Nocodazole (Fig. 2 A). In both cases, most microtubules were depolymerized and only a few short microtubules remained at the centrosome (Fig. 2 A and Fig. S3 A). Although these few

microtubules could not interact with the cell periphery, nor with most of the intracellular space, the centrosomes displayed a robust stationary behavior and remained near the centroid of the cells over a time course of several hours (Fig. 2, B and C). Because this phenomenon could result from the anchoring of the centrosome to the nucleus, we repeated these experiments in cytoplasts and confirmed the ability of "mini-asters" to remain well-centered in the absence of any interactions with the nucleus (Fig. 2, D and E). These findings further demonstrated that microtubules were not required to maintain the centrosome at the center of the cell. In light of the results from our laser ablation experiments, we then tested whether the actin network could be the primary actor responsible for the integration of the entire cell volume in the centering process. Cells were cotreated with Nocodazole (6 μM) and Cytochalasin D (0.5 μg/ml) to block the assembly of actin filaments and disrupt most actin-based structures. This treatment could not be applied to cytoplasts without inducing their detachment, but a significant proportion of the cells could remain at least partially spread. After 6 h of treatment with Nocodazole and Cytochalasin D, centrosome positions were largely randomized and a few centrosomes could even be observed at the very edge of the cells (Fig. 2, F and G). The dispersion relative to cell size was even more striking (Fig. 2 H) since cells treated with Cytochalasin D were smaller than control cells (Fig. S3 B). Centrosome mispositioning appeared to result from independent drifts in both the positions of the centrosome and the centroid of the cell (Fig. 2 I). We wondered to what extent centrosomal positioning could be explained by random behavior within the accessible cellular volume. To explore this possibility, we compared its positioning to the dispersion of Golgi apparatus fragments induced by microtubule disassembly (Fig. S3 C). As long as the actin network remained intact, the asters lay significantly closer to the centroid of the cells than the Golgi fragments. However, upon actin disruption, asters and fragments followed the same distribution, thereby highlighting the random positioning of centrosomes in this context (Fig. S3, D and E). Overall, the integrity of the actin network, and not that of the microtubule network, appeared to
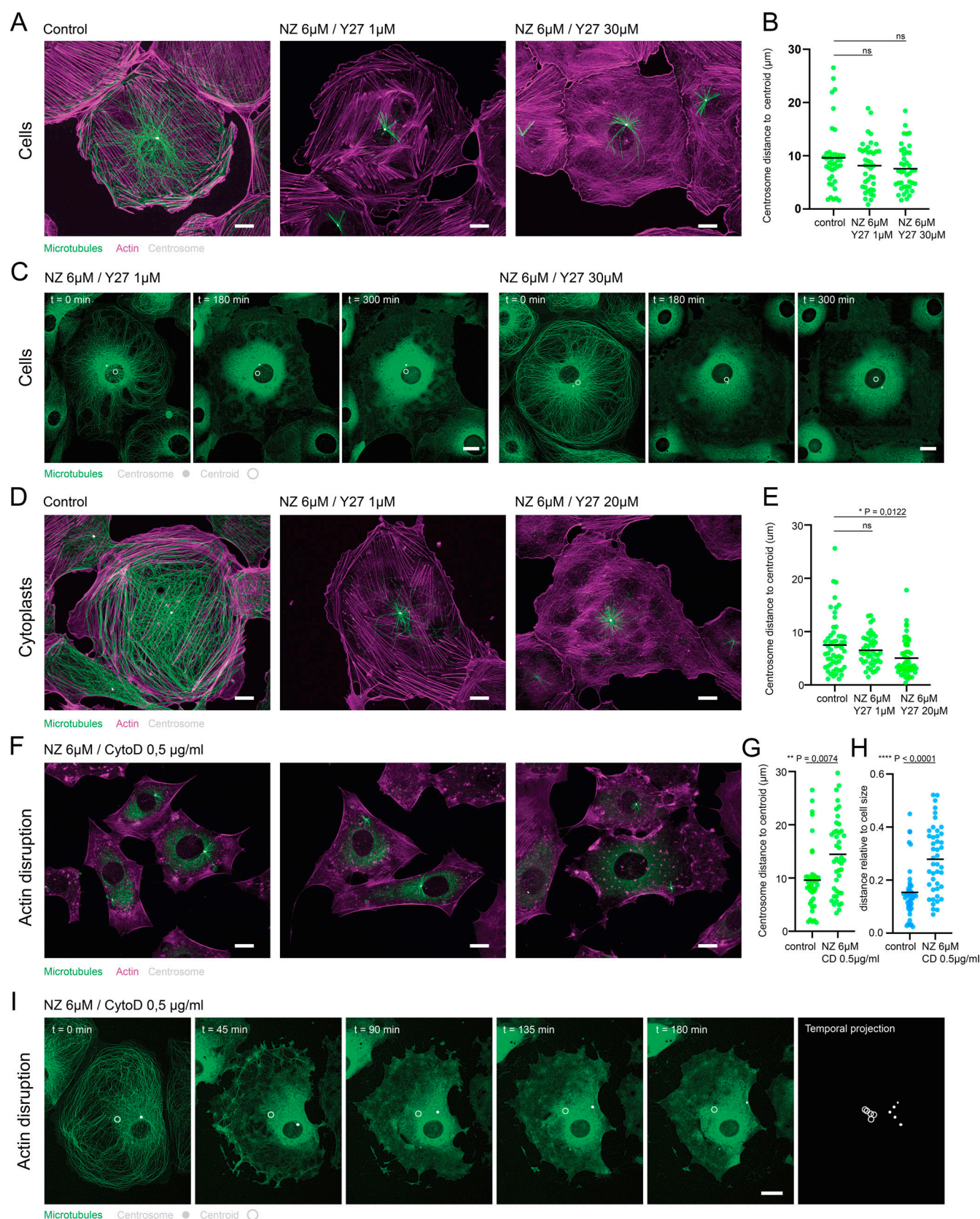
Figure 2.   Respective role of actin filaments and microtubules networks in centrosome positioning. (A–I) Mini-aster positioning in PtK2 cells (A–C and F–I) and cytoplasts (D and E) expressing GFP-tubulin. **(A)** Images show the actin filaments (magenta), microtubules (green), and centrosome (white) in a non-treated PtK2 cell (left), a cell treated with 6 µM of Nocodazole and 1 µM of Y27632 (middle) or 30 µM of Y27632 (right). **(B)** Graph representing the distance between the centrosome and the centroid of the cell in the control (*n* = 40), the highly (*n* = 40), and poorly (*n* = 41) contractile cells. **(C)** Representative live

acquisitions depicting the stationary positions of the centrosome and the centroid during the establishment of mini-asters inside PtK2 cells. Generation of a mini-aster in a strongly contractile cell (Nocodazole 6 µM and Y27632 1 µM) (left); generation of a mini-aster inside a poorly contractile cell (Nocodazole 6 µM and Y27632 30 µM) (right). **(D)** Images show the actin filaments (magenta), microtubules (green), and centrosome (white) in a PtK2 cytoplast (left), a cytoplast treated with 6 µM of Nocodazole and 1 µM of Y27632 (middle) or 20 µM of Y27632 (right). **(E)** Graph representing the distance between the centrosome and the centroid of the cytoplast in the control ($n = 55$), the highly ($n = 45$), and the poorly ($n = 51$) contractile cytoplast conditions. **(F)** Images show the actin filaments (magenta), microtubules (green), and centrosome (white) in a PtK2 cell treated with Nocodazole (6 µM) and Cytochalasin D (0.5 µg/ml). **(G)** The graph shows the distance between the centrosome and the centroid of the cell in the control ($n = 40$) and Cytochalasin D and Nocodazole cotreated condition ($n = 44$). **(H)** The graph shows the centrosome distance to the centroid normalized by cell size (i.e., divided by the square root of the area of the cell) in the control ($n = 40$) and Cytochalasin D and Nocodazole co-treated condition ($n = 44$). **(I)** Live acquisition depicting the independent drifts of the centrosome and the centroid during the generation of a mini-aster within a cell with a disrupted actin network (Nocodazole 6 µM and Cytochalasin D 0.5 µg/ml). **(A, D, and F)** All images are max projections, further processed using an unsharp mask and a gamma filter, and in C and I, this process was followed by background subtraction. In the graphs, horizontal bars represent the mean. P represents the P values, which were obtained from Kruskal–Wallis non-parametric tests (B and E) or Mann–Whitney non-parametric tests (G and H). Scale bars are 10 µm.

be necessary for the maintenance of the centrosome near the center of adherent cells.

These results seemed to contradict previous studies concluding that microtubules play a role in the generation and transmission of forces that regulate aster centering in adherent cells (Wu et al., 2011; Hale et al., 2011; Zhu et al., 2010). This includes our own observation of centrosome mispositioning in response to dynein inactivation by the overexpression of a dominant negative form of the p150 subunit of dynactin (Jimenez et al., 2021). We wondered whether the long-term effects of protein knockdown in previous experiments and the short duration of our laser ablations or drug treatments might reveal a difference between the establishment and the maintenance of centrosome centration. The specific study of the establishment of centration inside adherent cells is challenging because it requires starting from a clearly off-centered position, which is hard to observe in normal conditions. Fortunately, we were able to take advantage of an intermediate stage of the enucleation protocol: just after the centrifugation step, and before the washout of the cytoskeletal drugs that were necessary to weaken cell architecture and allow cell fragmentation, where the centrosome lies close to the cytoplast's periphery. By removing all the drugs used during the enucleation process (Cytochalasin D, Y27632, and Nocodazole), the microtubule and actin networks could recover their architectures (Fig. S4, A and B) and the centrosomes moved away from cell periphery toward the center of the cytoplasts within 4 h (Fig. 3 A). Interestingly, by washing out actin drugs only and keeping the Nocodazole, we were able to observe the contribution of the actin network in the absence of microtubules to the centration process (Fig. 3 B; and Fig. S4, A and B). In this condition, centrosome centering was still possible but incomplete (13 µm distance to the center as compared to 8 µm in control conditions, Fig. 3, A and B). Centrosomes were moved at the same speed and with the same directionality as when microtubules were present (Fig. S4, C and D). The mechanism driving centrosome displacement was probably non-specific. Indeed, non-functionalized fluorescent beads underwent centration with the same kinetics and trajectories as the centrosomes (Fig. S4, E and F). This shows that the actin network is able to drive centration independently of microtubules.

Unfortunately, the exact opposite conditions, i.e., repositioning in the presence of microtubules and in the absence of the actin network, could not be studied. After washing out

Nocodazole only and keeping the Cytochalasin D, the cytoplasts could not remain spread out and detached rapidly. We therefore designed another approach to assess the ability of a microtubule network to center autonomously a centrosome. By replacing the enucleation buffer with the actin "freezing" buffer immediately after enucleation and washing out the Nocodazole, we were able to test the ability of microtubules to recenter the centrosome within a static actin network (Fig. S4, A and B). Despite normal microtubule regrowth, the asters failed to recenter (Fig. 3 C). Microtubules spanned the entire cytoplasm, but the forces produced by their polymerization dynamics, or by molecular motors acting on them, were not sufficient to move the asters against actin filaments, leading to the striking assembly and maintenance of highly off-centered microtubule networks (Fig. 3 D). Overall, our results show that the actomyosin network can center the centrosome through a non-specific centripetal flow. Microtubules are neither necessary for generating and controlling this displacement nor capable of driving it independently through the actin meshwork (Fig. 3 E).

Counterintuitively, even though the absolute displacements of the centrosome were strictly similar in the presence or absence of microtubules (Fig. 3 F and Fig. S4 D), recentering was much more efficient in the control condition (dynamic actin and microtubule networks) than in the absence of microtubules (in the presence of Nocodazole) (Fig. 3 G). This suggests that centrosome displacement is not the only factor contributing to centrosome centering, and although microtubules are inconsequential for maintaining centering, they may play a role in centrosome centration.

Careful observation of cytoplast behavior upon washing out of cytoskeletal drugs after enucleation revealed that centrosome centering was not simply driven by centrosome displacement. In fact, the cytoplasts moved and reorganized their shapes around the centrosome. The centrosome and the centroid appeared to converge toward each other (Fig. 4 A and Video 9). This prompted us to further quantify the relative contributions of both the displacement of the centroid (i.e., the reorganization of the cell shape around the centrosome) and the displacement of the centrosome to the final centering precision (Fig. 4 B). A first striking observation was that, on average, the motion of the centroid was responsible for nearly 50% of the centering process (Fig. 4 C). Unexpectedly, a closer look at the individual recentering events revealed that smaller distance errors between the centrosome and the centroid (i.e., good centering events)
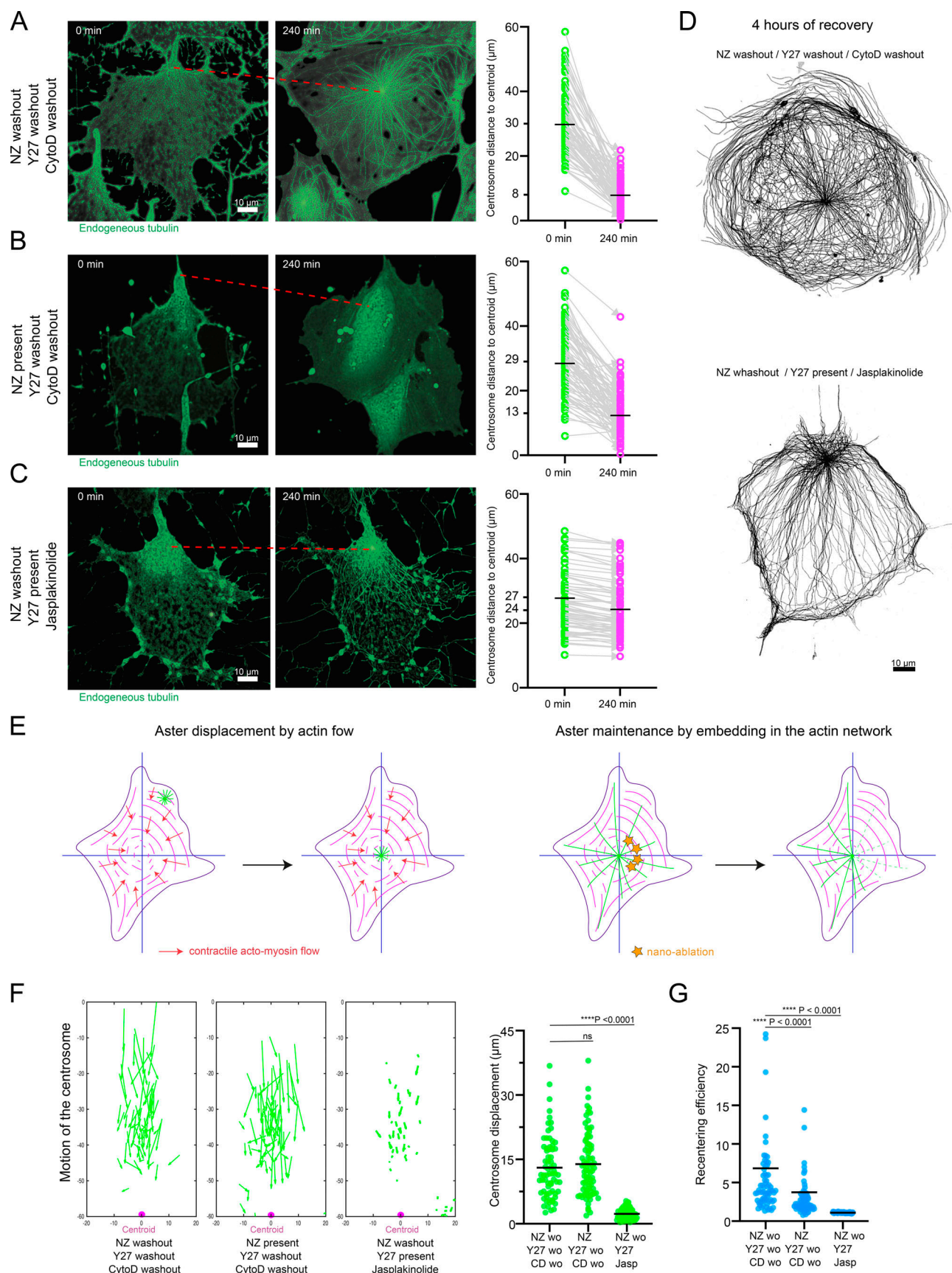
Figure 3. Centrosome recentering following cell enucleation. PtK2 cells expressing GFP-tubulin were enucleated in the presence of Nocodazole (10 µM), Y27632 (10 µM), and Cytochalasin D (3 µg/ml). After enucleation and before the removal of the enucleation drugs, all cytoplasts displayed a damaged actin

network and an off-centered centrosome biased in the direction of the enucleation pull. The contributions of actin and microtubules in the recentering processes were investigated by washing out one or the other drug. **(A)** The image sequence shows microtubule network recovery upon Nocodazole, Y27632, and Cytochalasine-D washout (n = 70). The dotted red curve highlights the motion of the centrosome. The graph shows the distance separating the centrosome and the centroid before and 4 h after drug washout. **(B)** Image sequence showing microtubule network recovery upon Y27632 and Cytochalasine-D washout (n = 70). Nocodazole is still present. The dotted red curve highlights the motion of the centrosome. The graph shows the distance separating the centrosome and the centroid before and 4 h after drug washout. **(C)** Image sequence showing microtubule network recovery upon Nocodazole washout in the presence of Y27632 (20 μM) and Jasplakinolide (600 nM) (n = 66). The graph shows the distance separating the centrosome and the centroid before and 4 h after drug washout. **(D)** Images illustrate a well-centered microtubule aster 4 h after Nocodazole, Y27632, and Cytochalasine-D washout (top), and a non-centered aster upon Nocodazole washout in the presence of Y27632 (20 μM) and Jasplakinolide (600 nM) (bottom). **(E)** Schematic depiction of the nonspecific centration of the centrosomal aster through the centripetal actomyosin flow and its latter maintenance near the center of the cell through its embedding inside the actomyosin network. **(F)** Vectorial plots depicting the displacement of the centrosomes toward the centroid of the cytoplasts in the three different centrosome recentering conditions (left). Graph representing the total displacement of the centrosomes in the three different centrosome recentering conditions (right). **(G)** Graph representing the recentering ratio (i.e., the ratio between the final and initial distances separating the centrosome and the centroid) in the three different centrosome recentering conditions. **(A–C)** Live images were processed following the described pipeline in the Materials and methods section. **(D)** Images are max projections that were further processed using an unsharp mask and a gamma filter. In the graphs, horizontal bars represent the mean. P represents the P values, which were obtained from Kruskal–Wallis non-parametric tests.

---

appeared to be associated with displacements of the centroid larger than the displacements of the centrosome (Fig. 4 C). Indeed, the displacement of the centrosome was not correlated to the final distance error (Fig. 4 D). On the other hand, the accuracy of the final centration of the centrosome was correlated to the displacement of the centroid, i.e., to the ability of cytoplasts to reorganize themselves around the centrosome (Fig. 4 E). In a few cases, we could even observe centrosome centering in the absence of any significant centrosome displacement (Fig. 4 F). Hence, centrosome centering appears to be more dependent on the reorganization of the cytoplasm around the centrosome than on centrosome displacement itself. This led us to formulate a new hypothesis that could reconcile earlier observations on the role of microtubules and dyneins in the control of centrosome centering with our own observations (Wu et al., 2011; Hale et al., 2011; Zhu et al., 2010; Jimenez et al., 2021). Although microtubules appear unable to generate forces strong enough to drive centrosome motion through the actin network of adherent cells, they could direct cell reorganization around the centrosome by guiding the transport of cell mass or by delivering remodeling signals to the actin network. This prompted us to further examine the role of microtubules and dyneins in this particular mechanism.

We first tested the impact of dynein-based forces on the maintenance of the centrosome at the cell center by injecting a blocking antibody against dynein (74.1, Dillman and Pfister, 1994) in PtK2 and RPE1 cells. This led to a clear dispersion of the Golgi apparatus (Fig. S5 A) (Yi et al., 2011). However, it did not affect the position of the centrosome (Fig. S5, B, C, E, and F), even though we could observe an important perturbation of the pericentrosomal microtubule network with a loss of its astral organization (Fig. S5, D and G) (Quintyne et al., 1999). In agreement with our previous experiments showing the dispensability of microtubules in centering maintenance, these additional results showed that dynein-based forces were not required for the maintenance of the central position of the centrosome in adherent cells. Unfortunately, this experimental strategy could not be used to study the centering process since the probability to properly enucleate and recover injected cells was extremely low after enucleation. We thus opted for the overexpression of a dominant-negative form of the dynactin

subunit p150 glued (p150-DN) (Quintyne et al., 1999; Wu et al., 2018), which was also associated with a strong dispersal of the Golgi apparatus (Fig. S5 H). As expected from earlier work (Jimenez et al., 2021), the microtubule networks appeared disorganized and centrosomes adopted more random positions (Fig. 5 A). We then performed recentering experiments inside enucleated PtK2 cells expressing the p150–DN–GFP construct while keeping both the actin and microtubule network dynamics (Nocodazole washout, Y27632 washout, and Cytochalasin D washout). Akin to cells, cytoplasts expressing p150–DN–GFP displayed perturbed microtubule networks and abnormally positioned centrosomes (Fig. 5 B). Although the absolute distance of centrosome displacement was not impacted, recentering efficiency was significantly lower than in the control, and the final centration was much less precise (Fig. S5 I). Interestingly, this reduced efficiency was similar to the one observed in the absence of microtubules (Fig. S5 I). Importantly, when monitoring the motion of the centroid in freshly enucleated cytoplasts (Fig. 5 C), we noticed that in the absence of microtubules and in the presence of microtubules but absence of dynein activity, the displacements of cytoplasts centroids toward the centrosome were impaired in a very similar way (Fig. 5 D). Particularly, both the magnitude (Fig. 5 D) and the orientation (Fig. 5 E) of the centroid displacements were affected, leading to a final defect in centrosome recentering without impacting centrosomal motion itself (Fig. 4 G and Fig. S5 I). These two sets of experiments, conducted in the absence of microtubules or in their presence but without dynein activity, showed that microtubules contribute to centrosome centering by guiding dynein-dependent cell reorganization around the centrosome (Fig. 5 F).

Taken together, our data reveal that centrosome positioning in adherent cells is supported by two synergistic mechanisms: the centripetal actomyosin flow that drags the centrosome toward the cell center (Fig. 3 E) and the redistribution of cell mass around the centrosome by dynein-based transport along microtubules (Fig. 5 F).

Importantly, we show that tension and pressure along microtubules cannot lead to effective displacements of the centrosome and that the microtubule asters in adherent cells are submitted to high resistive forces due to their embedding in the network of actin filaments. These conclusions suggest that the
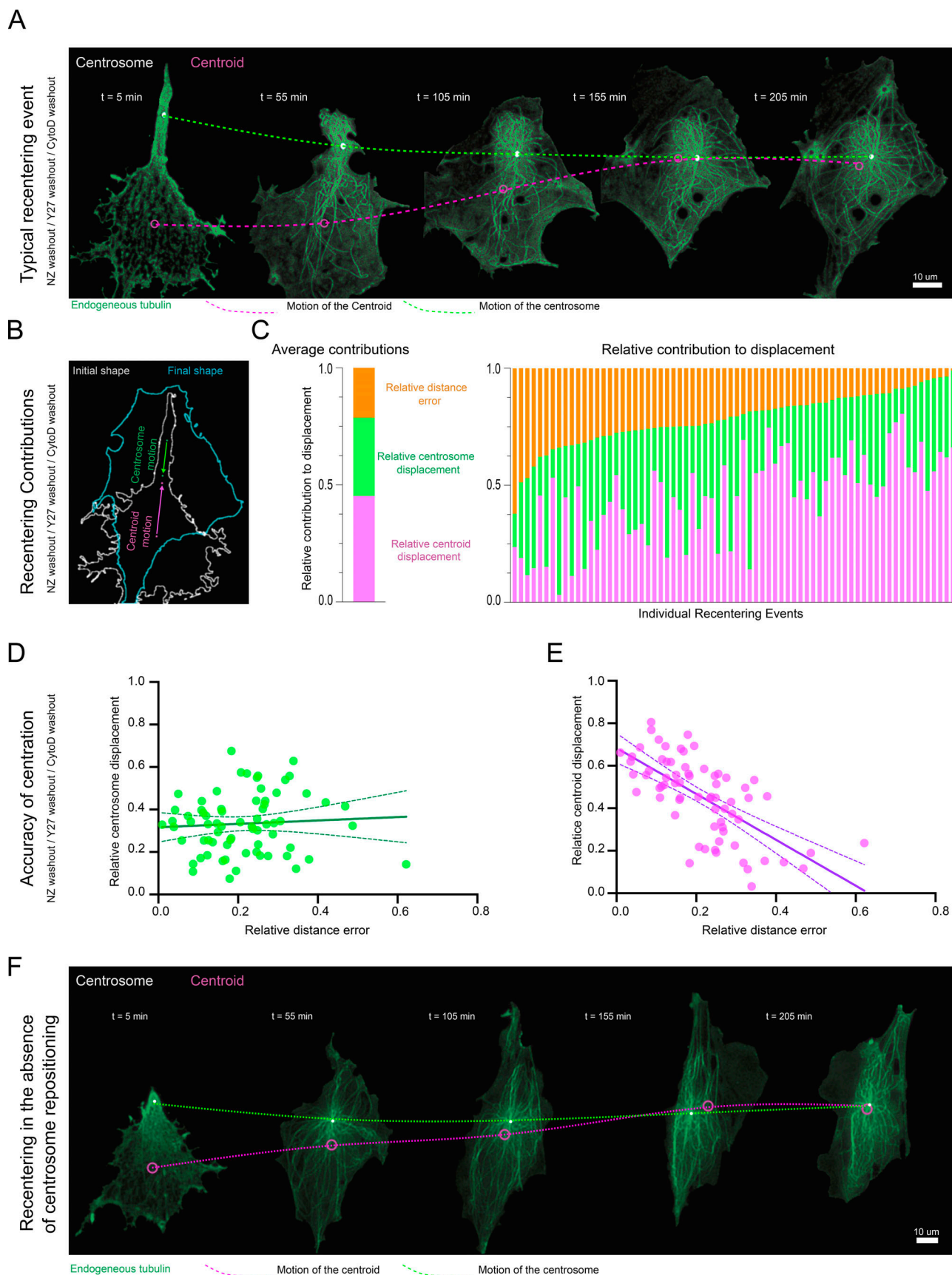
Figure 4. **Cell shape remodeling around the centrosome.** Centrosome recentering in the control condition (Nocodazole washout, Y27632 washout, Cytochalasin D washout) in PtK2 cytoplasts expressing GFP-tubulin (*n* = 70). **(A)** Five selected time points of a representative live centrosome recentering event

showing the repositioning of the centrosome and the centroid inside a cytoplast over a time course of a few hours. The dotted green line underscores the motion of the centrosome, and the dotted magenta line underscores the motion of the centroid. **(B)** The left image shows the overlay of the first and last time points of the recentering event depicted in A. The arrows represent the magnitude and direction of the centrosome and the centroid total displacements. The error corresponds to the final distance between the centrosome and the centroid. **(C)** The left graph shows the average relative contributions of the displacements of the centrosomes and the centroid to the recentering events upon the washout of all the drugs. The right graph shows the relative distance measurements in 80 individual recentering events sorted by final error. Distances are normalized to the initial distance separating the centrosome and the centroid. **(D)** The graph shows the correlation between centrosome displacement and the distance error. Distances are normalized to the initial distance separating the centrosome and the centroid. (dark green line represents the best linear fit, dotted green line represents the fit's 95% confidence interval). **(E)** Same as D but showing the correlation between the displacement of the centroid and the distance error. **(F)** Example of a centrosome recentering event. Here, recentering occurs almost exclusively through the repositioning of the centroid inside the cytoplast over a time course of a few hours. The dotted green line underscores the motion of the centrosome, and the dotted magenta line underscores the displacement of the centroid. **(A and F)** Images were processed following the described pipeline in the dedicated Materials and methods section.

radial organization of microtubules around the centrosome is actually a consequence of the isotropic and persistent growth of microtubules from the centrosome rather than a mechanism regulating centrosome positioning through a force balance along microtubules. Consequently, the irregular shapes of microtubules and their anisotropic spatial distributions actually reflect the physical constraints on their growth in a dense and heterogeneous cytoplasm and do not impair the mechanism of aster positioning.

The extent to which microtubule mechanics contribute to the position of the microtubule aster seems to depend on the size and shape of the cell in relation to the architecture of the actin network. In adherent cells, microtubules are embedded inside a dense actin network, which generates a mechanical coupling that prevents autonomous displacements of the microtubule aster (Orii and Tanimoto, 2025). In contrast, in mammalian eggs or mitotic cells, the actin network is more concentrated along the periphery than in the cytoplasm in a way that could decrease the constraints on microtubules (Rosa et al., 2015; Tanimoto et al., 2016). These conditions might be more favorable for the propagation of forces along microtubules and the displacement of the aster. According to this view, the degree of freedom of the microtubule aster is inversely correlated to the density of the actin network and thereby more or less sensitive to external cues. Interestingly, this role of actin can be modulated and offers a degree of control that can change aster positioning accordingly. Indeed, actin disassembly can facilitate centrosome displacement throughout the cytoplasm during ciliogenesis (Kim et al., 2010; Pitaval et al., 2010), as well as during immune synapse (Obino et al., 2015) or axon formation (Solecki et al., 2009). Actin network reorganization, concurrent with mitotic cell rounding, decreases cytoplasmic density and strengthens the cortical network, which frees the microtubules located near the cell center, allowing the emergence of their autonomous self-organization properties to form the mitotic spindle (Oriola et al., 2018) and allowing forces applied at the cortex to propagate up to spindle poles (Théry et al., 2007; Guild et al., 2017). The steric coupling between actin and microtubule networks can also be reduced by other means such as the release of microtubules from the centrosome to allow its translocation by molecular motors (Hannaford et al., 2022). Therefore, various mechanisms of cytoplasmic clearance or aster disassembly exist, which can modulate the constraints imposed by the actin network on microtubule aster positioning.

Our findings also indicate that the microtubule network guides the constant redistribution of the cell mass around the centrosome from which it radiates (Fig. 5 F). We found that dyneins were key in this regulation. It is still unclear whether dyneins actively transport the cell mass and thereby bring to the centrosome the cell components that are the most distant from it, or whether they transport signals, which further modulate cell shape reorganization. These signals, which remained to be identified, could also be directly associated with microtubules, which may serve as sensors and signaling platforms, guiding the dynamics of the actin network (Verma and Maresca, 2019; Wasteneys, 2004; Parker et al., 2014). This biochemical regulation of the actin network by microtubules opens the possibility for an interesting morphogenetic loop between actin-based steric forces on the microtubule aster and microtubule-based biochemical modulation of actin network dynamics and contraction. Indeed, biochemical signals associated with microtubules, such as GEF-H1, could promote myosin contraction and actin network retraction (Rafiq et al., 2019) and thus reduce the longest distances between the cell edge and the centrosome. Alternatively, other signals, such as APC, could promote the growth of actin filaments and the formation of membrane protrusions (Efimova et al., 2020), leading to an increase in the distance between the cell edge and the centrosome. Hence, depending on the nature of the biochemical coupling between microtubules and actin filaments, their interplay could either ensure a robust centering or an active decentering of the centrosome. It is tempting to hypothesize that such a biochemical conversion could drive centrosome decentering toward the rear as cells become motile (Zhang et al., 2017; Mastrogiovanni et al., 2020; Sánchez-Madrid and Serrador, 2009; Burute et al., 2017). We hope that these results and speculations will promote further investigations of the biochemical coupling between microtubules and the network of actin filaments in the maintenance or break of cell symmetry.

Materials and methods

See Table S1 for the references of all reagents.

Cell culture

PtK2 (*Potorous tridactylus* kidney) cells (control or stably expressing GFP-α-tubulin) (Khodjakov et al., 2003) were obtained from the lab of Franck Perez (Institut Curie, Paris, France) and
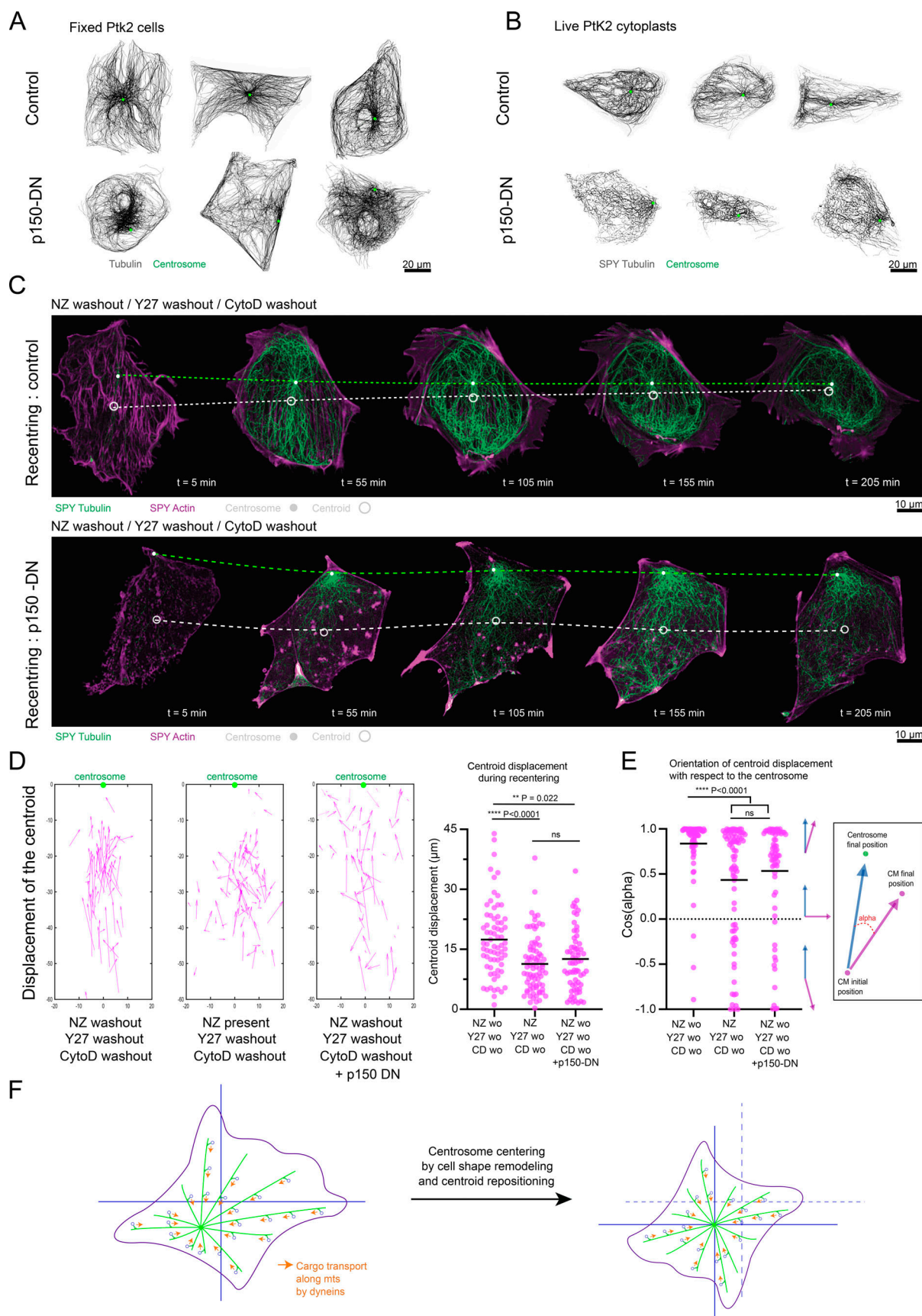
Figure 5. Microtubules and dyneins direct cell shape remodeling around the centrosome. (A) Images show the microtubule network (gray) and the centrosome (green) in PtK2 cells not expressing p150–DN–GFP (top) or expressing p150–DN–GFP (bottom). **(B)** Live images of the microtubule network (gray)

and the centrosome (green) in PtK2 cytoplasts, expressing (bottom) or not (top) p150–DN–GFP, a few hours after the total washout of the enucleation drugs. In A and B, images are max projections further processed using an unsharp mask, an enhance contrast filter, a gamma filter, and a background subtraction filter. **(C)** Selected time points of representative live centrosome recentering events showing the repositioning of the centrosome and the centroid over a time course of a few hours after the total washout of the enucleation drugs. Images show the recentering in a PtK2 cytoplast not expressing p150–DN–GFP (top), or expressing p150–DN–GFP (bottom). The dotted green line underscores the motion of the centrosome, and the dotted white line underscores the motion of the centroid. Images were processed following the described pipeline in the dedicated Materials and methods section. **(D)** Vectorial plots depicting the displacement of the centroid toward the centrosome (left), graph representing the magnitude of the displacement of the centroid (right) in the three different centrosome recentering conditions: (1) Nocodazole washout, Y27632 washout, Cytochalasin D washout (n = 70); (2) Nocodazole present, Y27632 washout, Cytochalasin D washout (n = 81), (3) expression of p150–DN–GFP construct and Nocodazole washout, Y27632 washout, Cytochalasin D washout (n = 67). **(E)** Graph shows the cosine of the angle between the vectors connecting the initial positions of the centrosome and the centroid, and the trajectory of the centroid in the three different centrosome recentering conditions. In D and E, horizontal bars represent the mean. P represents the P values, which were obtained from Kruskal–Wallis non-parametric tests. **(F)** Schematic depiction of the centrosomal aster and its associated dynein molecular motors guiding the repositioning of the cell body around the centrosome.

were not further characterized. Human telomerase–immortalized RPE1 (retinal pigmental epithelial) cells were initially purchased from ATCC by Michel Bornens and were not further characterized. Mouse embryonic fibroblast (MEF) cells (immortalized by stable expression of SV40 large T antigen) generated by the lab of John Eriksson (Virtakoivu et al., 2015) were a gift from the lab of Robert Goldman (Northwestern University, Evanston, IL, USA) (Patteson et al., 2019). They were not further characterized.

Cells were grown at 37°C and 5% CO_2 in DMEM/F12 supplemented with 10% fetal bovine serum and 1% of antibiotic–antimycotic solution (Thermo Fisher Scientific). Upon passage, cells were detached using TrypLE (Thermo Fisher Scientific).

Beads endocytosis
20 µl of 500 nm red fluorospheres solution was pipetted and centrifuged for 15 min at 13,000 g at room temperature inside an Eppendorf microcentrifuge equipped with an FA-24 rotor. After centrifugation, the supernatant was discarded and the bead pellet was resuspended using 1 ml of culture medium. Classically, PtK2 cells were cultivated in T-75 culture flasks filled with 10 ml of culture medium. When cells were cultivated in the presence of beads, 500 µl of the resuspended bead solution was added to 9.5 ml of culture medium. Cells were kept for a day or two in the presence of the beads to ensure sufficient endocytosis before the experiments.

Cell transfection
For p150 inhibition assays during centrosome recentering in cytoplasts, we used control PtK2 cells instead of cells expressing GFP–tubulin to avoid confusion between the GFP from the tubulin and from the p150 construct. PtK2 cells were transfected with the plasmid expressing GFP–p150–CC1 (214–548 aa of p150Glued) (Wu et al., 2018) obtained from Mineko Kengaku (Kyoto University, Kyoto, Japan) using Lipofectamine 2000 (11668027; Thermo Fisher Scientific) in serum and antibiotic-free culture media.

Drug treatments
Live actin and microtubule staining
Actin and microtubules were labeled in live imaging using SIR-Actin/SPY FastAct and SPY-Tubulin. The labeling reagents were added directly to the cell culture media for at least 2 h prior to imaging and were not washed before the acquisitions. SPY-Tubulin and SPY-FastAct were used at a dilution of 1/1,000 and SiR-Actin was used at a concentration of 300 nM. To further improve the quality of the live stainings, we performed all the labeling in the presence of Verapamil (10 µM).

Actin "freezing"
To fully immobilize the actin network, cytoplasts were treated with a combination of Jasplakinolide (600 nM) and Y27632 (20 µM). The incubation was performed either after the full recovery of the cytoplasts or right after enucleation and lasted for at least 2 h.

Mini-asters
PtK2 cells stably expressing GFP-tubulin were detached and platted on square 20 × 20 polystyrene slides coated with fibronectin and collagen (both at 21 µg/ml) and placed inside an incubator for at least 24 h. PtK2 cytoplasts expressing GFP-tubulin, enucleated in the context of intact microtubule asters, were left for 4 h in the incubator to recover. Cells or cytoplasts were then submitted to various drug treatments for 6 h prior to fixation and labeling: Nocodazole (6 µM) with Y27632 (1 µM) to obtain the high contractility state, Nocodazole (6 µM) with Y27632 (30 µM) (or 20 µM for cytoplasts) to obtain the low contractility state, or Nocodazole (6 µM) with Cytochalasin D (0.5 µg/ml) to mildly depolymerize actin.

Fragmentation of the Golgi apparatus
PtK2 cells stably expressing GFP-tubulin were detached and platted on square 20 × 20 polystyrene slides coated with fibronectin and collagen (both at 21 µg/ml) and placed inside an incubator for at least 24 h. Cells or cytoplasts were then submitted to various drug treatments for at least 6 h prior to fixation and labeling: Nocodazole (6 µM) with Y27632 (1 µM) to obtain the distribution of Golgian fragments in the high contractility state, Nocodazole (6 µM) with Y27632 (30 µM) to obtain the distribution of Golgian fragments in the low contractility state, or Nocodazole (6 µM) with Cytochalasin D (0.5 µg/ml) to obtain the distribution of Golgian fragments in the context of a mildly depolymerized actin network.

Cell enucleation
Cells were detached and platted on square 20 × 20 polystyrene slides coated with fibronectin and collagen (both at 21 µg/ml) and placed inside an incubator for at least 12 h. Prior to

enucleation, cells were incubated for 20 min at 37°C in an enucleation buffer (Cytochalasin D, +/− Y27632, and +/− Nocodazole). Cells were then enucleated inside the enucleation buffer using high-speed centrifugation (13,000 RPM) for 25 min at 37°C. Enucleations were performed inside an Avanti JXN-26, Beckman Coulter centrifuge equipped with a swinging rotor (JS-13.1; Beckman Coulter). After enucleation, slides were rinsed with fresh culture media every 3 min for 12 min. Slides were then placed in the incubator for at least 4 h to allow for a complete recovery of the cytoplasts. Various pretreatment and enucleation buffers were used for the distinct cell types.

PtK2 cells stably expressing GFP-tubulin were submitted to an overnight treatment of Y27632 (5 μM). The enucleation buffer contained Cytochalasin D (3 μg/ml) and Y27632 (5 μM) (in culture media). To enucleate PtK2 with a mini-aster, cells were submitted to an overnight treatment of Nocodazole (10 μM) and Y27632 (10 μM). The enucleation buffer contained Cytochalasin D (3 μg/ml), Y27632 (10 μM), and Nocodazole (10 μM) (in culture media).

To enucleate PtK2 control cells with a mini-aster and follow centrosome recentering, cells were submitted to a 2-h treatment of Nocodazole (10 μM) and Y27632 (10 μM) followed by a to a 2 h treatment of Nocodazole (10 μM), Y27632 (10 μM), SPY-tubulin 555 (1/1,000), SPY-Fast-Act 647 (1/1,000), and Verapamil (10 μM). Cells were then transferred in an enucleation buffer containing Cytochalasin D (3 μg/ml), Y27632 (10 μM), Nocodazole (10 μM), SPY-tubulin 555 (1/1,000), SPY-Fast-Act 647 (1/1,000), and Verapamil (10 μM) (in culture media).

To enucleate RPE1 cells with a mini-aster, cells were not submitted to any overnight treatment prior to enucleation. The enucleation buffer contained Cytochalasin D (0.65 μg/ml), Y27632 (5 μM), and Nocodazole (5 μM) (in culture media).

To enucleate MEF cells with a mini-aster, cells were not submitted to any overnight treatment prior to enucleation. The enucleation buffer contained Cytochalasin D (0.35 μg/ml), Y27632 (10 μM), and Nocodazole (5 μM) (in culture media).

Centrosome recentering assay
PtK2 cells stably expressing GFP-tubulin were enucleated in the context of small microtubule asters. Right after enucleation, cytoplasts were directly brought to the microscope for imaging. After the first time point of the acquisition, the enucleation buffer was washed and replaced with fresh culture medium that could contain cytoskeletal drugs (Nocodazole [10 μM], Jasplakinolide [600 nM], and Y27632 [20 μM]) depending on the recentering condition.

Control PtK2 cells, expressing or not p150–DN–GFP, were enucleated in the context of small microtubule asters. Right after enucleation, cytoplasts were directly brought to the microscope for imaging. After the first time point of acquisition, the enucleation buffer was washed and replaced with fresh culture medium containing labeling reagents: SPY-tubulin 555 (1/1,000), SPY-Fast-Act 647 (1/1,000), and Verapamil (10 μM).

Live acquisitions lasted for 4 h with a 4-μm Z-stack (five steps spaced by 1-μm intervals) every 5 min. Depending on the acquisition, two or three (488 nm, 555 nm, ±647 nm) fluorescent channels were recorded.

Immunofluorescence
Cells were fixed for 10 min at room temperature in a cytoskeleton buffer (10 mM MES, 138 mM KCl, 3 mM MgCl, and 2 mM EGTA) supplemented with 10% sucrose, 0.05% Triton-X100, 0.05% glutaraldehyde, and 4% of paraformaldehyde. Aldehyde functions were then reduced using a $NaBH_4$ solution (1 mg/ml in PBS) for 10 min. The samples were then washed two times with PBS and one time with PBS-Tween 0.1%. The slides were then incubated in a blocking solution (PBS, 0.1% Tween-20, 3% BSA) for 25 min and then with the primary antibodies diluted in the blocking solution for 30 min. The slides were then rinsed three times using PBS-Tween 0.1% and incubated in a blocking solution for 30 min with secondary antibodies and labeled with phalloidin. Finally, the slides were rinsed two times in PBS-Tween 0.1%, one time in PBS, one time in milliQ water and then mounted in Mowiol 4–88.

Microtubules were stained using rat antibodies against tyrosinated tubulin (YL1/2, 1/300). Centrosomes were stained using either mouse antibodies against γ tubulin (1/300), rabbit antibodies against γ tubulin (1/300), or against pericentrin (1/300). The Golgi apparatus was stained using either mouse antibodies against GM130 (1/300) or rabbit antibodies against giantin (1/300). Actin was stained using phalloidin labeled with Alexa 488 (1/100). The secondary antibodies we used were donkey anti-rat Alexa 405 (A48268; Thermo Fisher Scientific), donkey anti-mouse Alexa 555 (A31570; Thermo Fisher Scientific), goat anti-mouse Alexa 405 (A31553; Thermo Fisher Scientific), and donkey anti-rabbit Alexa 647 (711-605-152; Jackson Immuno Research). The 74.1-antibody which was microinjected in cells was detected using a secondary anti-mouse antibody. When necessary, sequential stainings with primary and secondary antibodies were performed to use several mouse primary antibodies on the same cells.

Slides coating and patterning
Cleaning
Glass slides were submitted to three successive washing steps. First, slides were sonicated in acetone for 20–30 min. Then slides were sonicated in pure isopropanol for 20–30 min. Last, slides were sonicated in milliQ water for 20–30 min before being air dried.

Polystyrene coating
To promote cellular adhesion, glass slides were coated with a very thin layer of polystyrene. Clean slides were activated using a 3-min air plasma treatment (PE-50; plasmatech). The slides were then placed inside a semi-closed recipient heated at 75°C in the presence of a few drops of hexamethyldisilazane (HMDS) for at least 6 h. After HMDS treatment the slides were recovered and spin-coated with polystyrene. Briefly, the slides were mounted inside a spin coater (WS-650m2-23NPPB; Laurell), their surface was covered with a solution of 1% polystyrene (the polystyrene is dissolved in toluene), and subsequently spinned for 30 s at 1,500 rpm. After spin coating, the slides were collected, dried, and stored for a least 1 h prior to their use.

Protein coating
Polystyrene-coated slides were activated using air plasma treatment (PE - 50 plasmatech) for 45 s. After activation, the

slides were then placed inside a solution of proteins (12 or 21 µg/ml of fibronectin and collagen diluted in sterile PBS) for at least 30 min at room temperature. Slides were rinsed twice in milliQ water and once in sterile PBS.

Surface passivation
Polystyrene-coated slides were activated using air plasma treatment (PE - 50 plasmatech) for 45 s and immersed in a solution of 0.1 mg/ml of poly(L-Lysine)–poly(ethylene-glycol) (PLL–PEG; JenKemTechnology) in 10 mM Hepes (pH 7.4) for 1 h. PEGylated slides were briefly plunged into milliQ water and rapidly dewetted. The PLL–PEG slides were then stored at 4°C for at least 1 h.

Micropatterning
PEGylated coverslips were put in tight contact with a quartz-chrome printed photomask (Toppan Photomask). Tight contact was maintained using a vacuum holder. The PEG layer was burned with deep UV (190 nm) through the non-chromed windows of the photomask, using a UVO cleaner (Model No. 342A-220; Jelight), at a distance of 1 cm from the UV lamp with a power of 6 mW/cm², for 5 min. After exposure, the patterned PLL–PEG coated slides were gently detached from the mask by submerging them under milliQ water. Once the slides detached, they were dewetted and incubated in a solution of adhesion protein according to the protocol for protein coating.

Protein purification and labeling
Tubulin was purified from fresh bovine brain using three cycles of temperature-dependent assembly/disassembly in Brinkley Buffer 80 (BRB80: 80 mM Pipes pH 6.8, 1 mM EGTA and 1 mM MgCl$_2$) (Vantard et al., 1994). MAP-free neurotubulin was subsequently purified by cation exchange chromatography (EMD SO, 650 M; Merck) in 50 mM Pipes, pH 6.8, supplemented with 0.2 mM MgC1$_2$, and 1 mM EGTA. Fluorescently labeled tubulin (ATTO-565) was prepared by the following previously published method (Shelanski, 1973). Labeled tubulin later used for cellular microinjection was stored at −80°C inside a microinjection buffer (50 mM potassium glutamate, 1 mM MgCl$_2$, pH 6.8).

Actin was purified from rabbit skeletal-muscle acetone powder (Spudich and Watt, 1971). Monomeric Ca-ATP-actin was purified by gel-filtration chromatography on Sephacryl S-300 at 4°C in G buffer (2 mM Tris–HCl, pH 8.0, 0.2 mM ATP, 0.1 mM CaCl$_2$, 1 mM NaN$_3$ and 0.5 mM dithiothreitol [DTT]). Actin was labeled on lysines with Alexa 488 succinimidyl ester (Molecular Probes). Monomeric labeled actin later used for microinjection was typically stored concentrated (around 20–40 µM) and highly labeled (around 70%) inside 60% glycerol G-Buffer at −20°C.

Microinjection
Cells were detached and platted on polystyrene slides coated with fibronectin and collagen (both at 21 µg/ml) and placed inside an incubator for at least 12 h. Alternatively, cells were detached and platted on polystyrene patterned slides coated with fibronectin and collagen (both at 12 µg/ml) and placed inside an incubator for 12 h. Right before injection, the culture medium

was exchanged to remove dead cells and floating debris. Glass microneedles were pulled from Clark borosilicate thin wall capillary (30-0050; Harvard Apparatus) using a vertical pipet puller (PC-100; Narishige). Microneedles were manually controlled with an InjectMan 4 micromanipulator (Eppendorf). Microinjection of cells was performed on an inverted microscope (Nikon Ti2 Eclipse) equipped with a Prime BSI Express CMOS camera (Photometrics) and using a Nikon CFI Plan Fluor 40×/0.75 NA dry objective. Various compensation pressures were applied using a FemtoJet 4i (Eppendorf) pump. The cell medium was maintained at 37°C during the whole experiment using a H-301 heating chamber (Okolab). Micro-Manager 1.4.21 software was used for live image acquisition during the microinjection procedure. After microinjection, the cellular medium was exchanged and the cells were placed inside an incubator for a recovery period.

Tubulin speckles
Purified labeled tubulin was thawed on ice and diluted in injection buffer (50 mM potassium glutamate, 1 mM MgCl$_2$, pH 6.8) to obtain a final concentration of 1 µM. The obtained microinjection tubulin solution was kept on ice and protected from light. Microneedles were loaded with 10 µl of microinjection tubulin solution and connected to the Femtojet system. The compensation pressure used was set between 30 and 35 hPa. After microinjection, cellular media was exchanged and cells were placed inside an incubator for a 2-h recovery period.

Actin speckles
Purified labeled actin was diluted in injection buffer (50 mM potassium glutamate, 1 mM MgCl$_2$, pH 6.8) to obtain a final concentration of 1 µM. The obtained microinjection actin solution was kept on ice and protected from light. Microneedles were loaded with 10 µl of microinjection solution and were connected to the Femtojet system. The compensation pressure used was set between 70 and 90 hPa. After microinjection, the cellular medium was exchanged and cells were placed inside an incubator for a 2-h recovery period.

Actin and tubulin double speckle
Purified labeled actin and tubulin were diluted in injection buffer (50 mM potassium glutamate, 1 mM MgCl$_2$, pH 6.8) to obtain a final concentration of 1 and 1.5 µM, respectively. The obtained microinjection actin and tubulin solution was kept on ice and protected from light. Microneedles were loaded with 10 µl of microinjection solution and were connected to the Femtojet system. The compensation pressure used was set between 70 and 90 hPa. After microinjection, cellular media was exchanged and cells were placed inside an incubator for a 2-h recovery period.

Antibody against dyneins
Microneedles were loaded with 2 µl of the 74.1-antibody commercial solution and were connected to the Femtojet system. The compensation pressure used was set between 25 and 35 hPa. Cells were injected for 15 min and then placed inside the incubator for an incubation and recovery period of 50 min. After the

incubation period, cells were fixed and stained according to the immunofluorescence protocol. Injected cells were identified using a secondary anti-mouse antibody that recognized the 74.1 antibody.

Microscopy

Acquisitions were performed using a confocal spinning disk microscope (Nikon Ti Eclipse equipped with a spinning scanning unit CSU-X1 Yokogawa) and a R3 retiga camera (QImaging). Images were acquired using either Nikon CFI Plan Fluor 40×/1.3 NA oil objective, Nikon Plan Apo VC 60×/1.40 NA oil objective, and Nikon CFI Super Fluor 100×/1.3 NA oil objective. Each wavelength was acquired separately. Metamorph software was used for images acquisition. Live acquisitions were performed inside a live module (kept at 37°C and 5% CO_2) mounted on the confocal spinning disk microscope. In nearly all live acquisitions, Hepes (1 M, pH 7.4) (1/100) and Oxyfluor (1/100) were added to the culture media.

Laser-induced photodamage

Photoablation was performed on the aforementioned spinning-disc system from Nikon using the iLas2 device (Gataca Systems) equipped with a passively Q-switched laser (STV-E, Ream-Photonics) at 355 nm producing 500-ps pulses. Laser displacement, exposure time, and repetition rate were controlled via the ILas software interfaced with MetaMorph (Universal Imaging Corporation). Laser photoablations and subsequent imaging were performed with a CFI Super Fluor 100×/1.3 NA oil objective. Damages to the microtubule and actin networks were performed in parallel to image acquisition using the single spot ON-FLY function. This allowed for a high flexibility and live definition of the localizations of laser ablation events. The laser power used was set to 15% and the spot length was set to 500. Consequences of microtubule network ablations on centrosome position were monitored by recording a 2-μm Z-stack around the focal plane of the centrosome every 10 s.

Image processing and analysis

Most image processing and analysis were performed using the Fiji software. Additional processing and analysis were performed using MATLAB.

Centrosome detection and tracking

Z-stacks of γ tubulin immunostainings were projected onto a single plane. Centrosome position was extracted using the "Find maxima" plugin.

In living cells, Z-stacks of GFP-tubulin or SIR-tubulin were projected onto a single plane and further processed using a Gaussian filter (Sigma-Aldrich = 2 pixels). The centrosomal area was manually thresholded and the centroid of this area was defined as the position of the centrosome. Centrosome tracking was performed using the "Trackmate" plugin in Fiji. Tracks were constructed using the simple LAP tracking algorithm. Tracking parameters were finely tuned for each centrosome tracking event.

In ablation experiments, centrosome displacements away from the ablated region were counted positively. Temporal projection of centrosomal absolute displacements onto a single axis linking the centrosome and the centroid of the ablated area were performed with MATLAB (see Fig. S1).

To generate the vectorial map of centrosome displacements during recentering, all the images were realigned on the final position of the centroid of the cytoplasts. The graphs were plotted using the MATLAB "Quiver plot" tool, and the vectors were scaled by a factor of 0.5.

Microtubule network analysis

Z-stacks of the microtubule network were projected onto a single plane and subsequently semiautomatically segmented to generate a mask. The area of this mask was used as a proxy for the size of the microtubule network.

In ablation experiments, only the microtubules on the side of the centrosome where the ablation occurred were considered. See the graphical representation in Fig. S1 for the geometrical definition of the microtubule network disruption region and its quantification. The microtubule network was projected onto a single plane, and the total intensity along a line crossing the considered centrosomal microtubules was interpreted as the initial number of microtubules on this side of the centrosome prior to laser ablation. Along this same line, the total intensity of ablated microtubules was measured. The microtubule depletion ratio was computed as the ratio of the total fluorescence of ablated microtubules over the total fluorescence of all considered microtubules.

Actin and tubulin speckles detection and tracking

First, speckle images were cleaned using the "Subtract background" function in Fiji. Then, the "Normalized local contrast" integral filter was applied. To remove the additional noise created by this processing, a "Gaussian blur filter" coupled to a manual intensity subtraction were then used. Finally, another Gaussian blur filter was applied to quench the remaining noise (Fig. S2).

Segmented speckles were tracked using the "Trackmate" plugin of Fiji. Tracks were constructed using the "simple LAP tracking" algorithm (Fig. S2). Tracking parameters were finely tuned for each tracking event. A total period of 15 or 30 s centered on the ablation event was defined to analyze the behavior of the actin filaments or microtubules. The periods before and after ablation were each composed of six frames and shared a common frame (the frame right before ablation). Only tracks lasting for the entire period were considered. The total displacements of the tracks were extracted and averaged.

The reconstituted speckle tracks were imported into MATLAB to compute the displacement vectors between the first and last positions of the speckle in each individual tracks. The displacement vectors were then plotted using the "Quiver plot" tool.

Cell shape analysis

In fixed cells or cytoplasts, boundaries were defined using the phalloidin staining. In live cells or cytoplasts, boundaries were defined using GFP-tubulin or SPY-FASTACT-650. Z-stacks of the fluorescent signals were projected onto a single plane. The

contour of the cells or cytoplasts was extracted through manual thresholding of the images. The area and position of the centroid, in the segmented regions, were computed using the "Measure" function in Fiji.

To generate the vectorial map of centroid displacements, all the images were realigned on the final position of the centrosome. The graphs were plotted using the MATLAB "Quiver plot" tool and the vectors were scaled by a factor of 0.4.

Image processing of recentering events (Fig. 3, Fig. 4, and Fig. 5)

After a "Max Projection" of the entire volume of the cytoplasts, the microtubule channel was further processed using an "Unsharp mask." Additionally, to facilitate the visualization of the cytoplasts' shapes, cytoplasts were segmented. Image portions that were not contained inside the cytoplasts' segmented masks were removed.

Statistical analysis

Graph design and statistical analysis were performed on GraphPad PRISM. Inside our statistical analysis, normal distribution was not assumed. Statistical differences were computed using nonparametric methods. To assess the difference between the two groups, we employed two-tailed Mann–Whitney statistical tests. To assess the differences between three groups or more, we employed Kruskal–Wallis statistical tests. Statistical significance is indicated as follows: *$P < 0.05$, **$P < 0.01$, ***$P < 0.001$, ****$P < 0.0001$. All statistical tests and their P values are indicated in the corresponding figures.

Online supplemental material

Fig. S1, Fig. S2, Video 1, Video 2, Video 3, Video 4, Video 5, Video 6, Video 7, and Video 8 show additional data for Fig. 1. Fig. S3 shows additional data for Fig. 2. Fig. S4 shows additional data for Fig. 3. Video 9 shows additional data for Fig. 4. Fig. S5 shows additional data for Fig. 5. Table S1 provides a list of all the commercial products used in this work.

Data availability

Data (raw images and quantifications of centroid and centrosome positions) are available upon reasonable request.

References

Arquint, C., A.M. Gabryjonczyk, and E.A. Nigg. 2014. Centrosomes as signalling centres. *Philos. Trans. R. Soc. Lond. B Biol. Sci.* 369:20130464. https://doi.org/10.1098/rstb.2013.0464

Azoury, J., K.W. Lee, V. Georget, P. Rassinier, B. Leader, and M.-H. Verlhac. 2008. Spindle positioning in mouse oocytes relies on a dynamic meshwork of actin filaments. *Curr. Biol.* 18:1514–1519. https://doi.org/10.1016/j.cub.2008.08.044

Bornens, M. 2008. Organelle positioning and cell polarity. *Nat. Rev. Mol. Cell Biol.* 9:874–886. https://doi.org/10.1038/nrm2524

Brangwynne, C.P., G.H. Koenderink, F.C. Mackintosh, and D.A. Weitz. 2008. Nonequilibrium microtubule fluctuations in a model cytoskeleton. *Phys. Rev. Lett.* 100:118104. https://doi.org/10.1103/PhysRevLett.100.118104

Brangwynne, C.P., F.C. MacKintosh, S. Kumar, N.A. Geisse, J. Talbot, L. Mahadevan, K.K. Parker, D.E. Ingber, and D.A. Weitz. 2006. Microtubules can bear enhanced compressive loads in living cells because of lateral reinforcement. *J. Cell Biol.* 173:733–741. https://doi.org/10.1083/jcb.200601060

Brangwynne, C.P., F.C. MacKintosh, and D.A. Weitz. 2007. Force fluctuations and polymerization dynamics of intracellular microtubules. *Proc. Natl. Acad. Sci. USA.* 104:16128–16133. https://doi.org/10.1073/pnas.0703094104

Burakov, A.V., and E.S. Nadezhdina. 2020. Centering and shifting of centrosomes in cells. *Cells.* 9:1351. https://doi.org/10.3390/cells9061351

Burakov, A., E. Nadezhdina, B. Slepchenko, and V. Rodionov. 2003. Centrosome positioning in interphase cells. *J. Cell Biol.* 162:963–969. https://doi.org/10.1083/jcb.200305082

Burute, M., M. Prioux, G. Blin, S. Truchet, G. Letort, Q. Tseng, T. Bessy, S. Lowell, J. Young, O. Filhol, and M. Théry. 2017. Polarity reversal by centrosome repositioning primes cell scattering during epithelial-to-mesenchymal transition. *Dev. Cell.* 40:168–184. https://doi.org/10.1016/j.devcel.2016.12.004

Chaigne, A., C. Campillo, N.S. Gov, R. Voituriez, J. Azoury, C. Umaña-Diaz, M. Almonacid, I. Queguiner, P. Nassoy, C. Sykes, et al. 2013. A soft cortex is essential for asymmetric spindle positioning in mouse oocytes. *Nat. Cell Biol.* 15:958–966. https://doi.org/10.1038/ncb2799

Chaigne, A., C. Campillo, R. Voituriez, N.S. Gov, C. Sykes, M.-H. Verlhac, and M.-E. Terret. 2016. F-actin mechanics control spindle centring in the mouse zygote. *Nat. Commun.* 7:10253. https://doi.org/10.1038/ncomms10253

Colin, A., G. Letort, N. Razin, M. Almonacid, W. Ahmed, T. Betz, M.E. Terret, N.S. Gov, R. Voituriez, Z. Gueroui, and M.-H. Verlhac. 2020. Active diffusion in oocytes nonspecifically centers large objects during prophase I and meiosis I. *J. Cell Biol.* 219:e201908195. https://doi.org/10.1083/jcb.201908195

de-Carvalho, J., S. Tlili, T.E. Saunders, and I.A. Telley. 2024. The positioning mechanics of microtubule asters in Drosophila embryo explants. *Elife.* 12:RP90541. https://doi.org/10.7554/eLife.90541

Dillman, J.F. III, and K.K. Pfister. 1994. Differential phosphorylation in vivo of cytoplasmic dynein associated with anterogradely moving organelles. *J. Cell Biol.* 127:1671–1681. https://doi.org/10.1083/jcb.127.6.1671

Efimova, N., C. Yang, J.X. Chia, N. Li, C.J. Lengner, K.L. Neufeld, and T.M. Svitkina. 2020. Branched actin networks are assembled on microtubules by adenomatous polyposis coli for targeted membrane protrusion. *J. Cell Biol.* 219:e202003091. https://doi.org/10.1083/jcb.202003091

Farhadifar, R., C.-H. Yu, G. Fabig, H.-Y. Wu, D.B. Stein, M. Rockman, T. Müller-Reichert, M.J. Shelley, and D.J. Needleman. 2020. Stoichiometric interactions explain spindle dynamics and scaling across 100 million years of nematode evolution. *Elife.* 9:e55877. https://doi.org/10.7554/eLife.55877

Field, C.M., and P. Lénárt. 2011. Bulk cytoplasmic actin and its functions in meiosis and mitosis. *Curr. Biol.* 21:R825–R830. https://doi.org/10.1016/j.cub.2011.07.043

Garzon-Coral, C., H.A. Fantana, and J. Howard. 2016. A force-generating machinery maintains the spindle at the cell center during mitosis. *Science.* 352:1124–1127. https://doi.org/10.1126/science.aad9745

Grill, S.W., J. Howard, E. Scha, E.H.K. Stelzer, and A.A. Hyman. 2003. The distribution of active force generators controls mitotic spindle position. *Science.* 301:518–521. https://doi.org/10.1126/science.1086560

Grill, S.W., and A.A. Hyman. 2005. Spindle positioning by cortical pulling forces. *Dev. Cell.* 8:461–465. https://doi.org/10.1016/j.devcel.2005.03.014

Guild, J., M.B. Ginzberg, C.L. Hueschen, T.J. Mitchison, and S. Dumont. 2017. Increased lateral microtubule contact at the cell cortex is sufficient to drive mammalian spindle elongation. *Mol. Biol. Cell.* 28:1975–1983. https://doi.org/10.1091/mbc.e17-03-0171

Hale, C.M., W.-C. Chen, S.B. Khatau, B.R. Daniels, J.S.H. Lee, and D. Wirtz. 2011. SMRT analysis of MTOC and nuclear positioning reveals the role of EB1 and LIC1 in single-cell polarization. *J. Cell Sci.* 124:4267–4285. https://doi.org/10.1242/jcs.091231

Hannaford, M.R., R. Liu, N. Billington, Z.T. Swider, B.J. Galletta, C.J. Fagerstrom, C. Combs, J.R. Sellers, and N.M. Rusan. 2022. Pericentrin interacts with Kinesin-1 to drive centriole motility. *J. Cell Biol.* 221:e202112097. https://doi.org/10.1083/jcb.202112097

Hannaford, M.R., and N.M. Rusan. 2024. Positioning centrioles and centrosomes. *J. Cell Biol.* 223:e202311140. https://doi.org/10.1083/jcb.202311140

Haupt, A., and N. Minc. 2018. How cells sense their own shape - mechanisms to probe cell geometry and their implications in cellular organization and function. *J. Cell Sci.* 131:jcs214015. https://doi.org/10.1242/jcs.214015

Hooikaas, P.J., H.G.J. Damstra, O.J. Gros, W.E. van Riel, M. Martin, Y.T.H. Smits, J. van Loosdregt, L.C. Kapitein, F. Berger, and A. Akhmanova. 2020. Kinesin-4 KIF21B limits microtubule growth to allow rapid centrosome polarization in T cells. *Elife.* 9:e62876. https://doi.org/10.7554/eLife.62876

Jimenez, A.J., A. Schaeffer, C. De Pascalis, G. Letort, B. Vianay, M. Bornens, M. Piel, L. Blanchoin, and M. Théry. 2021. Acto-myosin network geometry defines centrosome position. *Curr. Biol.* 31:1206–1220.e5. https://doi.org/10.1016/j.cub.2021.01.002

Khodjakov, A., L. Copenagle, M.B. Gordon, D.A. Compton, and T.M. Kapoor. 2003. Minus-end capture of preformed kinetochore fibers contributes to spindle morphogenesis. *J. Cell Biol.* 160:671–683. https://doi.org/10.1083/jcb.200208143

Kim, J., J.E. Lee, S. Heynen-Genel, E. Suyama, K. Ono, K. Lee, T. Ideker, P. Aza-Blanc, and J.G. Gleeson. 2010. Functional genomic screen for modulators of ciliogenesis and cilium length. *Nature.* 464:1048–1051. https://doi.org/10.1038/nature08895

Kimura, K., and A. Kimura. 2011. A novel mechanism of microtubule length-dependent force to pull centrosomes toward the cell center. *Bioarchitecture.* 1:74–79. https://doi.org/10.4161/bioa.1.2.15549

Koonce, M.P., J. Köhler, R. Neujahr, J.M. Schwartz, I. Tikhonenko, and G. Gerisch. 1999. Dynein motor regulation stabilizes interphase microtubule arrays and determines centrosome position. *EMBO J.* 18:6786–6792. https://doi.org/10.1093/emboj/18.23.6786

Letort, G., F. Nedelec, L. Blanchoin, and M. Théry. 2016. Centrosome centering and decentering by microtubule network rearrangement. *Mol. Biol. Cell.* 27:2833–2843. https://doi.org/10.1091/mbc.E16-06-0395

Lombardi, M.L., D.E. Jaalouk, C.M. Shanahan, B. Burke, K.J. Roux, and J. Lammerding. 2011. The interaction between nesprins and sun proteins at the nuclear envelope is critical for force transmission between the nucleus and cytoskeleton. *J. Biol. Chem.* 286:26743–26753. https://doi.org/10.1074/jbc.M111.233700

Martin, M., and A. Akhmanova. 2018. Coming into focus: Mechanisms of microtubule minus-end organization. *Trends Cell Biol.* 28:574–588. https://doi.org/10.1016/j.tcb.2018.02.011

Mastrogiovanni, M., M. Juzans, A. Alcover, and V. Di Bartolo. 2020. Coordinating cytoskeleton and molecular traffic in T cell migration, activation, and effector functions. *Front. Cell Dev. Biol.* 8:591348. https://doi.org/10.3389/fcell.2020.591348

Meaders, J.L., S.N. de Matos, and D.R. Burgess. 2020. A pushing mechanism for microtubule aster positioning in a large cell type. *Cell Rep.* 33:108213. https://doi.org/10.1016/j.celrep.2020.108213

Meiring, J.C.M., B.I. Shneyer, and A. Akhmanova. 2020. Generation and regulation of microtubule network asymmetry to drive cell polarity. *Curr. Opin. Cell Biol.* 62:86–95. https://doi.org/10.1016/j.ceb.2019.10.004

Obino, D., F. Farina, O. Malbec, M. Maurin, P. Saez, M. Jouve, F. Dingli, D. Loewe, M. Yuseff, J. Gaillard, et al. 2015. Actin nucleation at the centrosome controls lymphocyte polarity. *Nat. Cell Biol.* 7:10969. https://doi.org/10.1038/ncomms10969

Orii, R., and H. Tanimoto. 2025. Structural response of microtubule and actin cytoskeletons to direct intracellular load. *J. Cell Biol.* 224:e202403136. https://doi.org/10.1083/jcb.202403136

Oriola, D., D.J. Needleman, and J. Brugués. 2018. The physics of the metaphase spindle. *Annu. Rev. Biophys.* 47:655–673. https://doi.org/10.1146/annurev-biophys-060414-034107

Parker, A.L., M. Kavallaris, and J.A. McCarroll. 2014. Microtubules and their role in cellular stress in cancer. *Front. Oncol.* 4:153. https://doi.org/10.3389/fonc.2014.00153

Patteson, A.E., A. Vahabikashi, K. Pogoda, S.A. Adam, K. Mandal, M. Kittisopikul, S. Sivagurunathan, A. Goldman, R.D. Goldman, and P.A. Janmey. 2019. Vimentin protects cells against nuclear rupture and DNA damage during migration. *J. Cell Biol.* 218:4079–4092. https://doi.org/10.1083/jcb.201902046

Pécréaux, J., S. Redemann, Z. Alayan, B. Mercat, S. Pastezeur, C. Garzon-Coral, A.A. Hyman, J. Howard, J. Pécréaux, S. Redemann, et al. 2016. The mitotic spindle in the one-cell C. elegans embryo is positioned with high precision and stability. *Biophys. J.* 111:1773–1784. https://doi.org/10.1016/j.bpj.2016.09.007

Pelletier, J.F., C.M. Field, S. Fürthauer, M. Sonnett, and T.J. Mitchison. 2020. Co-movement of astral microtubules, organelles and F-actin by dynein and actomyosin forces in frog egg cytoplasm. *Elife.* 9:e60047. https://doi.org/10.7554/eLife.60047

Peng, G.E., S.R. Wilson, and O.D. Weiner. 2011. A pharmacological cocktail for arresting actin dynamics in living cells. *Mol. Biol. Cell.* 22:3986–3994. https://doi.org/10.1091/mbc.E11-04-0379

Pitaval, A., Q. Tseng, M. Bornens, and M. Théry. 2010. Cell shape and contractility regulate ciliogenesis in cell cycle-arrested cells. *J. Cell Biol.* 191:303–312. https://doi.org/10.1083/jcb.201004003

Quintyne, N.J., S.R. Gill, D.M. Eckley, C.L. Crego, D.A. Compton, and T.A. Schroer. 1999. Dynactin is required for microtubule anchoring at centrosomes. *J. Cell Biol.* 147:321–334. https://doi.org/10.1083/jcb.147.2.321

Rafiq, N.B.M., Y. Nishimura, S.V. Plotnikov, V. Thiagarajan, Z. Zhang, S. Shi, M. Natarajan, V. Viasnoff, P. Kanchanawong, G.E. Jones, and A.D. Bershadsky. 2019. A mechano-signalling network linking microtubules, myosin IIA filaments and integrin-based adhesions. *Nat. Mater.* 18:638–649. https://doi.org/10.1038/s41563-019-0371-y

Rosa, A., E. Vlassaks, F. Pichaud, and B. Baum. 2015. Ect2/Pbl acts via Rho and polarity proteins to direct the assembly of an isotropic actomyosin cortex upon mitotic entry. *Dev. Cell.* 32:604–616. https://doi.org/10.1016/j.devcel.2015.01.012

Salmon, W.C., M.C. Adams, and C.M. Waterman-Storer. 2002. Dual-wavelength fluorescent speckle microscopy reveals coupling of microtubule and actin movements in migrating cells. *J. Cell Biol.* 158:31–37. https://doi.org/10.1083/jcb.200203022

Salpingidou, G., A. Smertenko, I. Hausmanowa-Petrucewicz, P.J. Hussey, and C.J. Hutchison. 2007. A novel role for the nuclear membrane protein emerin in association of the centrosome to the outer nuclear membrane. *J. Cell Biol.* 178:897–904. https://doi.org/10.1083/jcb.200702026

Sánchez-Madrid, F., and J.M. Serrador. 2009. Bringing up the rear: Defining the roles of the uropod. *Nat. Rev. Mol. Cell Biol.* 10:353–359. https://doi.org/10.1038/nrm2680

Scheer, U. 2014. Historical roots of centrosome research: Discovery of Boveri's microscope slides in Würzburg. *Philos. Trans. R. Soc. Lond. B Biol. Sci.* 369:20130469. https://doi.org/10.1098/rstb.2013.0469

Schuh, M., and J. Ellenberg. 2008. A new model for asymmetric spindle positioning in mouse oocytes. *Curr. Biol.* 18:1986–1992. https://doi.org/10.1016/j.cub.2008.11.022

Seetharaman, S., B. Vianay, V. Roca, A.J. Farrugia, C. De Pascalis, B. Boëda, F. Dingli, D. Loew, S. Vassilopoulos, A.D. Bershadsky, et al. 2021. Microtubules tune mechanosensitive cell responses. *Nat. Mater.* 21:366–377. https://doi.org/10.1038/s41563-021-01108-x

Shelanski, M.L. 1973. Chemistry of the filaments and tubules of brain. *J. Histochem. Cytochem.* 21:529–539. https://doi.org/10.1177/21.6.529

Solecki, D.J., N. Trivedi, E.-E.E. Govek, R.A. Kerekes, S.S. Gleason, and M.E. Hatten. 2009. Myosin II motors and F-actin dynamics drive the coordinated movement of the centrosome and soma during CNS glial-guided

neuronal migration. *Neuron*. 63:63–80. https://doi.org/10.1016/j.neuron .2009.05.028

Spudich, J.A., and S. Watt. 1971. The regulation of rabbit skeletal muscle contraction. I. Biochemical studies of the interaction of the tropomyosin-troponin complex with actin and the proteolytic fragments of myosin. *J. Biol. Chem.* 246:4866–4871. https://doi.org/10.1016/ S0021-9258(18)62016-2

Sulerud, T., A.B. Sami, G. Li, A. Kloxin, J. Oakey, and J. Gatlin. 2020. Microtubule-dependent pushing forces contribute to long-distance aster movement and centration in Xenopus laevis egg extracts. *Mol. Biol. Cell.* 31:2791–2802. https://doi.org/10.1091/mbc.E20-01-0088

Tang, N., and W.F. Marshall. 2012. Centrosome positioning in vertebrate development. *J. Cell Sci.* 125:4951–4961. https://doi.org/10.1242/jcs.038083

Tanimoto, H., A. Kimura, and N. Minc. 2016. Shape-motion relationships of centering microtubule asters. *J. Cell Biol.* 212:777–787. https://doi.org/10 .1083/jcb.201510064

Théry, M., A. Jiménez-Dalmaroni, V. Racine, M. Bornens, and F. Jülicher. 2007. Experimental and theoretical study of mitotic spindle orientation. *Nature*. 447:493–496. https://doi.org/10.1038/nature05786

Vantard, M., C. Peter, A. Fellous, P. Schellenbaum, and A.M. Lambert. 1994. Characterization of a 100-kDa heat-stable microtubule-associated protein from higher plants. *Eur. J. Biochem.* 220:847–853. https://doi.org/10 .1111/j.1432-1033.1994.tb18687.x

Verma, V., and T.J. Maresca. 2019. Microtubule plus-ends act as physical signaling hubs to activate RhoA during cytokinesis. *Elife*. 8:e38968. https://doi.org/10.7554/eLife.38968

Vignaud, T., C. Copos, C. Leterrier, M. Toro-Nahuelpan, Q. Tseng, J. Mahamid, L. Blanchoin, A. Mogilner, M. Théry, and L. Kurzawa. 2021. Stress fibres are embedded in a contractile cortical network. *Nat. Mater.* 20: 410–420. https://doi.org/10.1038/s41563-020-00825-z

Virtakoivu, R., A. Mai, E. Mattila, N. De Franceschi, S.Y. Imanishi, G. Corthals, R. Kaukonen, M. Saari, F. Cheng, E. Torvaldson, et al. 2015. Vimentin-

ERK signaling uncouples slug gene regulatory function. *Cancer Res.* 75: 2349–2362. https://doi.org/10.1158/0008-5472.CAN-14-2842

Wasteneys, G.O. 2004. Progress in understanding the role of microtubules in plant cells. *Curr. Opin. Plant Biol.* 7:651–660. https://doi.org/10.1016/j .pbi.2004.09.008

Wu, H.Y., G. Kabacaoğlu, E. Nazockdast, H.C. Chang, M.J. Shelley, and D.J. Needleman. 2024. Laser ablation and fluid flows reveal the mechanism behind spindle and centrosome positioning. *Nat. Phys.* 20:157–168. https://doi.org/10.1038/s41567-023-02223-z

Wu, J., G. Misra, R.J. Russell, A.J.C. Ladd, T.P. Lele, R.B. Dickinson, and A. Mogilner. 2011. Effects of dynein on microtubule mechanics and centrosome positioning. *Mol. Biol. Cell.* 22:4834–4841. https://doi.org/10 .1091/mbc.E11-07-0611

Wu, Y.K., H. Umeshima, J. Kurisu, and M. Kengaku. 2018. Nesprins and opposing microtubule motors generate a point force that drives directional nuclear motion in migrating neurons. *Development*. 145: dev158782. https://doi.org/10.1242/dev.158782

Xie, J., J. Najafi, R. Le Borgne, J.M. Verbavatz, C. Durieu, J. Sallé, and N. Minc. 2022. Contribution of cytoplasm viscoelastic properties to mitotic spindle positioning. *Proc. Natl. Acad. Sci. USA*. 119:e2115593119. https:// doi.org/10.1073/pnas.2115593119

Yi, J.Y., K.M. Ori-McKenney, R.J. McKenney, M. Vershinin, S.P. Gross, and R.B. Vallee. 2011. High-resolution imaging reveals indirect coordination of opposite motors and a role for LIS1 in high-load axonal transport. *J. Cell Biol.* 195:193–201. https://doi.org/10.1083/jcb.201104076

Zhang, J., Y. Wang, M. Théry, and H. Saint Louis. 2017. Centrosome defines the rear of cells during mesenchymal migration. *Mol. Biol. Cell.* 28: 3240–3251. https://doi.org/10.1091/mbc.E17-06-0366

Zhu, J., A. Burakov, V. Rodionov, and A. Mogilner. 2010. Finding the cell center by a balance of dynein and myosin pulling and microtubule pushing: A computational study. *Mol. Biol. Cell.* 21:4418–4427. https:// doi.org/10.1091/mbc.E10

Supplemental material
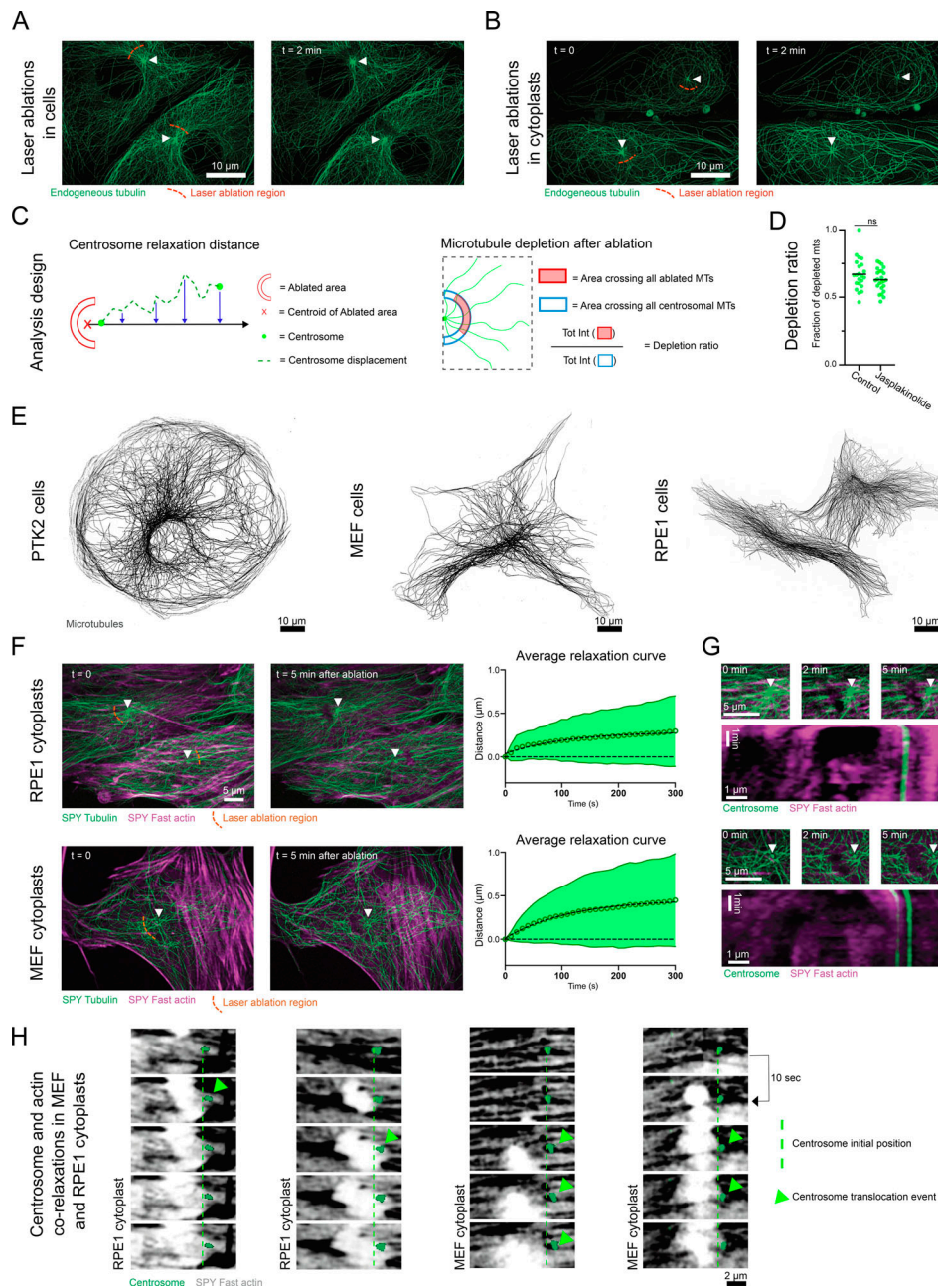
Figure S1. **Aster relaxation upon microtubule ablation in different cell types. (A)** First and last time points of a 2-min laser ablation experiment in PtK2 cells expressing GFP tubulin. A few microtubules were ablated on one side of the centrosome. The white triangular marks indicate the positions of the centrosomes. **(B)** First and last time points of a 2-min laser ablation experiment in PtK2 cytoplasts expressing GFP tubulin. A few microtubules were ablated on one side of the centrosome. The white triangular marks indicate the positions of the centrosomes. **(C)** Schematic representation of the quantifications of centrosome relaxation (left) and of the microtubule depletion ratio upon microtubule ablation (right). **(D)** The graph shows the proportion of depleted microtubules on the side of the centrosome, where the laser ablations were performed in the control condition (n = 22) and in the case of Jasplakinolide (600 nM) and Y27632 (20 µM) treatment (n = 24). Horizontal bars represent the mean. P values were obtained from a Mann–Whitney non-parametric test. **(E)** Images of the microtubule network in fixed PtK2 cells (left); MEF cells (middle); RPE1 cells (right). **(F)** Relaxation of the actin network (magenta) and microtubule network (green) upon repeated laser ablations during 5 min in RPE1 cytoplasts (top) and in MEF cytoplasts (bottom). White arrowheads indicate the positions of the centrosomes. Graphs show the mean relaxation profile of the centrosomes (30 RPE1 cytoplasts and 36 MEF cytoplasts). Circles represent the average displacement of the centrosome at each time point, the continuous lines represent the standard deviation. **(G)** Magnified view of the centrosomal area of an REP1 cytoplast (top) and a MEF cytoplast (bottom) depicted in Fig. S1 F. White arrows indicate the position of the centrosome. Kymograph representations of the centrosome and actin relaxations inside the zoomed-in areas. The kymographs (scaled three times to smoothen the signal) were performed along a straight line connecting the centrosomes with the centroids of the ablated areas and spanning the entire length of the zoomed-in areas. **(H)** Magnified views of the centrosomal areas during repeated laser ablation experiments in RPE1 and MEF cytoplasts. The temporal sequences are made of consecutive images covering a total period of 40 s. Small centrosomal translocation events can be visualized in parallel to local relaxations of the surrounding actin meshwork. **(A, B, E, and F)** All images are max projections, further processed using an unsharp mask and a gamma filter. **(H)** All images are max projections, further processed using a Gaussian blur filter. The LUT of the SPY FAST actin was inverted to facilitate the visualization of the local destruction and relaxation of the meshwork.

Schaeffer et al.
Two mechanisms of centrosome centration

Journal of Cell Biology   S2
https://doi.org/10.1083/jcb.202405126
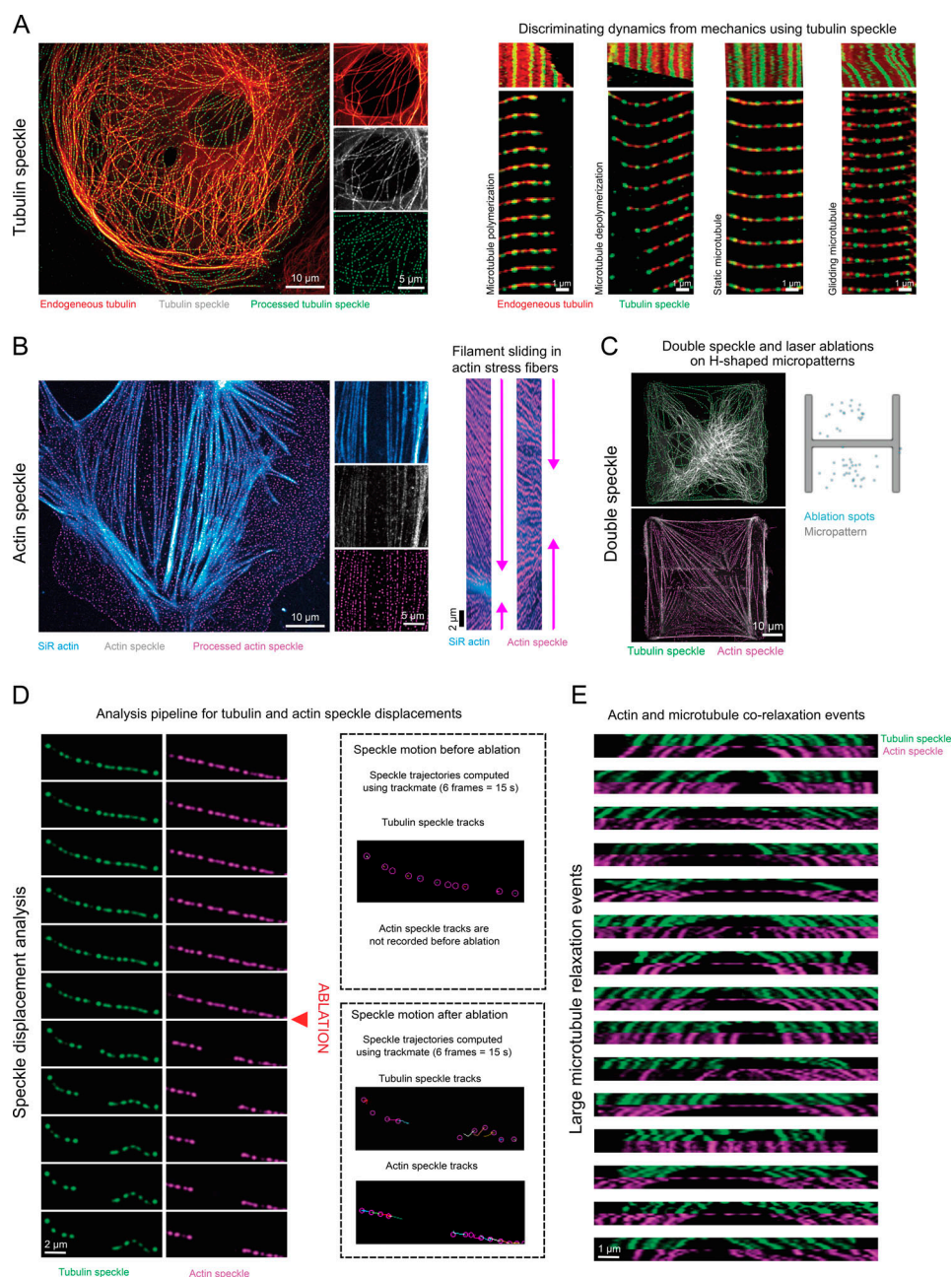
Figure S2. **Double-speckle microscopy and speckle tracking analysis. (A)** PtK2 cell expressing GFP-tubulin (red), 2 h after the microinjection of 1 μM purified Atto-555-tubulin (green). On the left, a representative live image of the microtubule network with the non-processed and processed tubulin speckles along the microtubules. On the right, kymographs (constructed over a period of 108 s) along the length of a few selected microtubules. Selected time points, extracted from the video used to build the kymograph, can be found below each corresponding kymograph. The reader can visualize a microtubule polymerizing, a microtubule depolymerizing, a static microtubule, and a microtubule gliding—kymographs are scaled by a factor of 3 for smoothness. **(B)** Control PtK2 cell stained using SIR-Actin (cyan), 2 h after microinjection of 1 μM labeled actin (Alexa 488) (magenta). On the left, a representative live image of the actin network with the non-processed and processed actin speckles along the actin structures. On the right, kymographs (constructed over a period of 30 min) along the length of two selected stress fibers. The reader can visualize contraction events with the presence of antiparallel speckles sliding along the length of both stress fibers—kymographs are scaled by a factor of 3 for smoothness. **(C)** Position of laser ablations in control PtK2 cells platted on 3,500 μm² patterns and co-injected 2 h earlier with purified and labeled actin and tubulin (1 and 1.5 μM respectively). Images show the tubulin (green) (top) and actin speckles (magenta) (bottom). The map shows the localizations of all the analyzed ablation events. **(D)** Analysis pipeline used to describe the behavior of a microtubule undergoing ablation. Briefly, the motions of the tubulin speckles were tracked 15 s before ablation and then again for 15 s after ablation using the simple LAP tracking method in Trackmate. When microtubules displayed significant relaxations, the motions of the surrounding actin speckles were tracked in parallel to that of the tubulin speckles. The amplitudes of the displacements of individual speckles were averaged to yield the mean amplitude of the displacement of the microtubule before and after ablation as well as the mean amplitude of the displacement of the surrounding actin meshwork after ablation. **(E)** Large microtubule relaxation events (motions >400 nm, depicted in Fig. 1 F). Kymographs showing the coordinated motions of the actin and tubulin speckles in the 15 s following laser ablation. The kymographs are constructed along the length of the moving microtubules and are scaled by a factor of 3 for smoothness. **(A–E)** For the details regarding actin and tubulin speckle processing, see the dedicated section in the Materials and methods.

Schaeffer et al.
Two mechanisms of centrosome centration

Journal of Cell Biology   S3
https://doi.org/10.1083/jcb.202405126
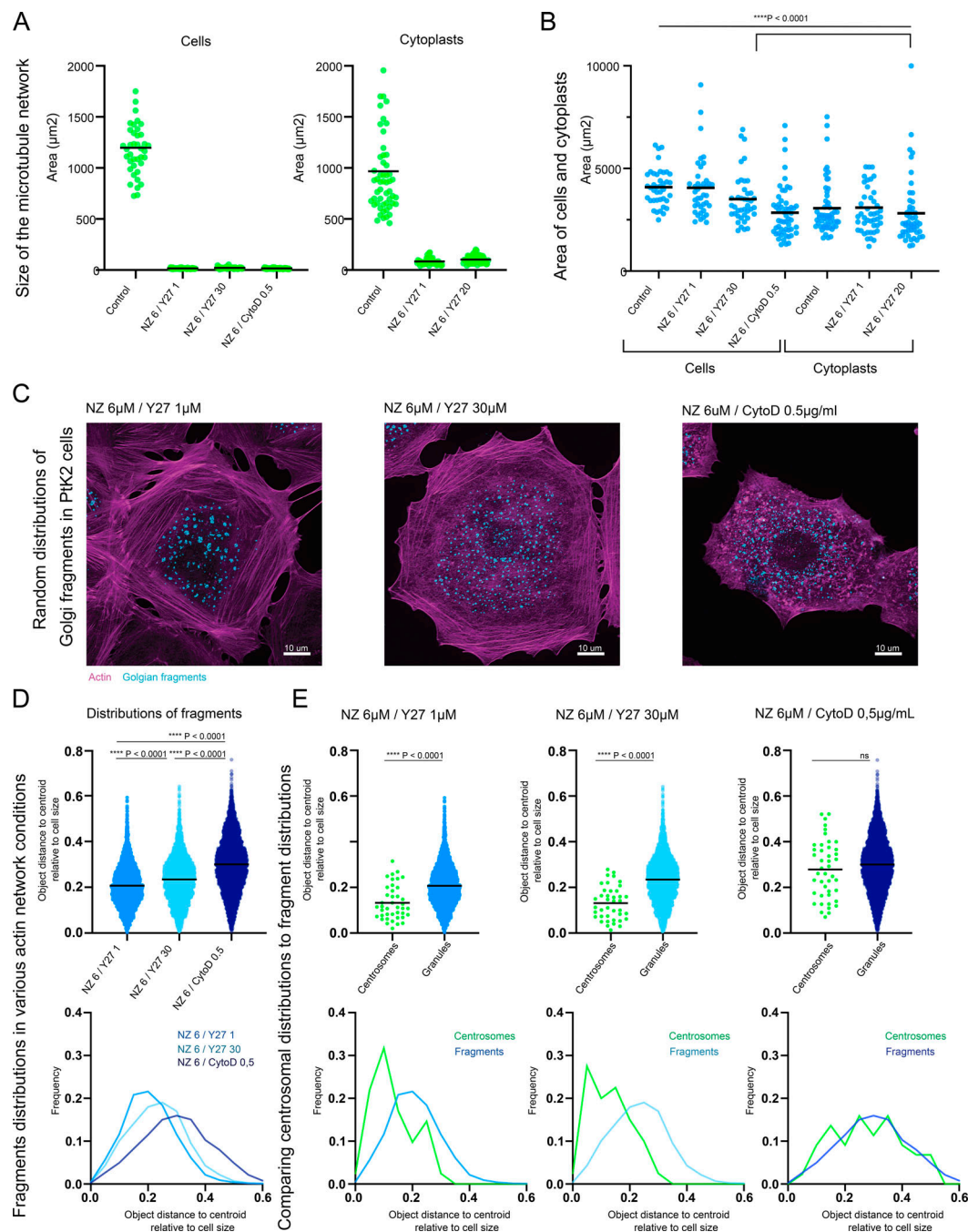
Figure S3. **Regulation of the positions of microtubule mini-asters and Golgi fragments. (A)** Graphs representing the size of the microtubule network in cells (left) and cytoplasts (right) in response to drug treatments: 6 h treatment of Nocodazole (6 µM) in parallel to Y27632 (1, 20, or 30 µM) or Cytochalasin D (0.5 µg/ml) to generate small microtubule asters in strongly contractile (NZ 6/Y27632 1, n = 41), poorly contractile (NZ 6/Y27632 30, n = 40), or disrupted actin networks (NZ 6/CytoD 0.5, n = 44). The size of the microtubule network was defined as the projected area occupied by the microtubule network (see the dedicated section inside the Materials and methods). **(B)** Graphs representing the spreading area of the cells (left) and cytoplasts (right) in response to drug treatments. The spreading area was determined using the actin signal. **(C)** Representative fixed images of the dispersion of Golgi fragments in various actin contexts. From left to right: clustered Golgi fragments in a strongly contractile actomyosin context (NZ 6 µM/Y27632 1 µM), wider dispersion of Golgi fragments in a poorly contractile actomyosin context (NZ 6 µM/Y27632 30 µM), and broad dispersion of Golgi fragments spanning the entire cytoplasm in a disrupted actin context (Nocodazole 6 µM/Cytochalasin D 0.5 µg/ml). All images are max projections, further processed using an unsharp mask and a gamma filter. **(D)** Quantifications of Golgi apparatus dispersal in conditions leading to mini-asters of microtubules. Top graph shows the distance of the Golgi fragments to the centroid normalized by cell size (square root of the area of the cell) in the various actin contexts. The bottom graph shows the frequency distributions of the distance of the Golgi fragments to the centroid relative to cell size (bottom). "NZ 6/Y27 1": n = 3,130 fragments, "NZ 6/Y27 30": n = 3,248 fragments, "NZ 6/Cyto D 0.5": n = 4,522 fragments. **(E)** The top graphs show the distance of the centrosome and the Golgi fragments to the centroid relative to cell size in response to the various drug treatments. The bottom graphs show the frequency distributions of the distance of the centrosome and the Golgi fragments to the centroid relative to cell size in response to the various drug treatments. In all graphs, horizontal bars represent the mean. P represents the P values, which were obtained from Kruskal–Wallis non-parametric tests (A, B, and D) or Mann–Whitney non-parametric tests (E).

Figure S4. Quantifications of centrosome recentering experiments. PtK2 cells expressing GFP-tubulin, which had endocytosed 500 nm fluorescently labeled non-functionalized polystyrene beads, were enucleated in the presence of Nocodazole (10 µM), Y27632 (20 µM) and Cytochalasin D (3 µg/ml). To challenge the contributions of actin and microtubules in the recentering process, we designed three washout experiments that were recorded over a period of 4 h. **(A and B)** Images of fixed cytoplasts. **(C and E)** Images from live cytoplasts. **(A)** Top: Images show well-centered microtubule asters after 4 h of all drugs washout. Middle: Images show small microtubule asters after 4 h of Y27632 and Cytochalasin D washout, i.e., in the presence of Nocodazole. Bottom: Images show off-centered microtubule asters 4 h after the washout of Nocodazole but in the presence of Y27632 and Jasplakinolide. **(B)** Images show the actin networks after 4 h of recentering. Left: Control conditions, i.e., Nocodazole washout, Y27632 washout, and Cytochalasin D washout. Middle: Nocodazole present, Y27632 washout, Cytochalasin D washout. Right: Nocodazole washout, Y27632 present, Jasplakinolide. **(A and B)** All images are max projections, further processed using an unsharp mask and a gamma filter. **(C)** Temporal projection of the successive positions of the centrosome during a representative recentering event in the presence of dynamic actin and microtubule networks. **(D)** Quantification of centrosome trajectories in the presence of dynamic microtubules (NZ washout, Y27632 washout, Cytochalasin D washout, $n = 70$) and in the absence of microtubules (Nocodazole present, Y27632 washout, Cytochalasin D washout, $n = 81$). From left to right, graphs represent the total distance traveled by the centrosomes during recentering (i.e., the sum of all their displacements and not the linear distance joining their initial and final positions), the average speeds at which the centrosomes moved during recentering, the frame-to-frame angular variation in centrosome motion during recentering, and the linearity of centrosome trajectories during recentering. Centrosome trajectories and their characteristics were extracted using the simple LAP tracking method in Trackmate. **(E)** Time-lapse sequences show the motions of centrosomes and endocytosed 500 nm beads over 4 h in the various recentering conditions. Kymographs show the coordinated displacements of the centrosome and the beads inside the zoomed-in region. The linescans were performed along a line following the trajectory of the centrosome and joining its initial and final positions. Images are max projections; the centrosome is further processed with an unsharp mask and a Gaussian blur. **(F)** Graphs comparing the centration of the centrosomes to that of fluorescent non-functionalized polystyrene beads after 4 h of recentering. Centrosomes ($n = 70$) and beads ($n = 471$) final centering in the presence of dynamic actin and microtubule networks (left). Centrosomes ($n = 81$), and beads ($n = 380$) final centering in the presence of a dynamic actin network but without microtubules (right). In the graphs, horizontal bars represent the mean. P represents the P values, which were obtained from Mann–Whitney non-parametric tests.

Schaeffer et al.
Two mechanisms of centrosome centration

Journal of Cell Biology S5
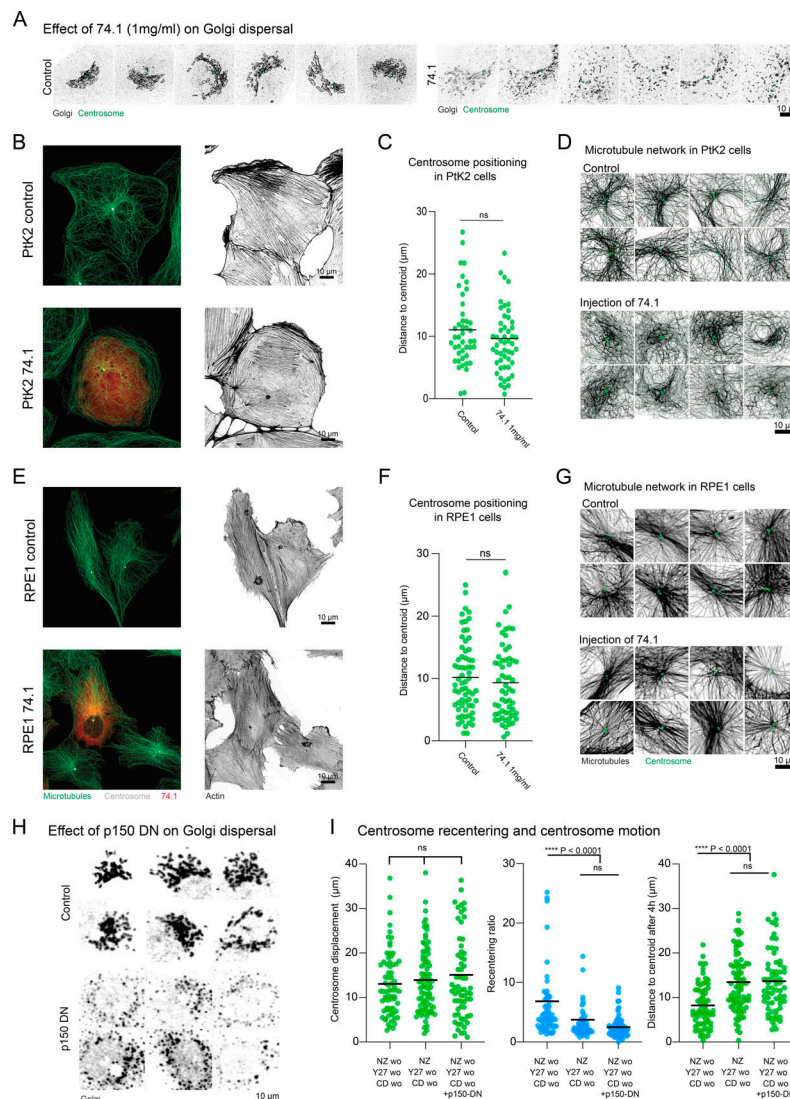https://doi.org/10.1083/jcb.202405126

Figure S5. **Effects of dynein inhibition on maintenance and establishment of centrosome centration. (A–G)** The activity of dynein molecular motors was inhibited inside Ptk2 and RPE1 cells through the microinjection of the 74.1 (1 mg/ml) inhibiting antibody. After microinjection, cells underwent a 50-min incubation period. In all the conditions, cells were fixed and stained for the microtubules, the centrosome, the Golgi apparatus, and actin. **(H)** Inhibition of dynein molecular motors activity inside control Ptk2 cells through the expression of a p150-DN construct. Cells were fixed 24 h after transfection and stained for the Golgi apparatus. **(I)** Three different centrosome recentering conditions. Two conditions inside PtK2 cytoplasts expressing GFP-tubulin: Nocodazole washout, Y27632 washout, Cytochalasin D washout (n = 70); Nocodazole present, Y27632 washout, Cytochalasin D washout (n = 81). One condition inside control PtK2 cytoplasts expressing the p150–DN–GFP construct: Nocodazole washout, Y27632 washout, Cytochalasin D washout (n = 67). In the graphs, horizontal bars represent the mean. P represents the P values, which were obtained from Kruskal-Wallis non-parametric tests (I) or Mann–Whitney non-parametric tests (C and F). **(A)** Effect of the injection of the 74.1 antibody on the morphology of the Golgi apparatus. Representative images of control Golgi apparatuses in fixed RPE1 cells (left). Representative images of Golgi apparatuses in fixed RPE1 cells 50 min after their microinjection with the 74.1 antibody (left). **(B)** Images of fixed PtK2 cells. Microtubule and actin networks in the control condition (top). Microtubule, and actin networks 50 min after the microinjection with the 74.1 antibody (bottom). **(C)** Effect of 74.1 microinjection inside PtK2 cells. Graph showing the distance between the centrosome and the centroid of the cell in the control (n = 44) and the 74.1 (n = 52) microinjected conditions. **(D)** Effect of the injection of 74.1 on the pericentrosomal microtubule network in PtK2 cells. Images of pericentrosomal networks in fixed control cells (top). Images of pericentrosomal networks 50 min after the microinjection with the 74.1 antibody (bottom). **(E)** Images of fixed RPE1 cells. Microtubule and actin networks in the control condition (top). Microtubule and actin networks 50 min after microinjection with the 74.1 antibody (bottom). **(F)** Effect of 74.1 microinjection inside RPE1 cells. Graph showing the distance between the centrosome and the centroid of the cell in the control (n = 66) and the 74.1 (n = 59) micro-injected conditions. **(G)** Effect of the injection of 74.1 on the pericentrosomal microtubule network in RPE1 cells. Images of pericentrosomal networks in control cells (top). Images of pericentrosomal networks 50 min after the microinjection with the 74.1 antibody (bottom). **(H)** Effect of p150-DN expression on the morphology of the Golgi apparatus. Images of Golgi apparatuses in fixed control PtK2 cells not expressing p150–DN–GFP. Images of Golgi apparatuses in fixed control Ptk2 cells 24 h after their transfection with p150-DN. **(I)** From left to right, the graph shows the total displacement of the centrosomes in the three different centrosome recentering conditions; graph showing the recentering ratio in the three different centrosome recentering conditions; graph showing the distance between the centrosome and the centroid at the end of the recentering experiments in the three different centrosome recentering conditions. **(A, B, D, E, and G)** All images are max projections, further processed using an unsharp mask and a gamma filter. **(H)** All images are max projections, further processed using an unsharp mask a gamma filter and a Gaussian blur filter.

Schaeffer et al.
Two mechanisms of centrosome centration

Journal of Cell Biology   S6
https://doi.org/10.1083/jcb.202405126

Video 1.   **Laser ablation experiment inside PtK2 cells expressing GFP tubulin (**Fig. S1**).** Microtubules appear in green. A few microtubules are ablated on one side of the centrosome and the motion of the centrosome is recorded using a confocal spinning disk microscope during the 2 min that follow ablation. A 2 µm wide Z-stack (spaced by 1 µm) is acquired every 10 s and is then MAX projected onto a single plane. Playback speed: 4 frames per second.

Video 2.   **Laser ablation experiment inside PtK2 cytoplasts expressing GFP tubulin (**Fig. S1**).** Microtubules appear in green. A few microtubules are ablated on one side of the centrosome and the motion of the centrosome is recorded using a confocal spinning disk microscope during the 2 min that follow ablation. A 2-µm wide Z-stack (three steps spaced by 1 µm) is acquired every 10 s and is then MAX projected onto a single plane. Playback speed: 4 frames per second.

Video 3.   **Repeated laser ablation experiment inside a PtK2 cytoplast expressing GFP tubulin (**Fig. 1**).** Microtubules (in green) are extensively and repeatedly depleted on one side of the centrosome for 5 min and the motion of the centrosome is recorded in parallel using a confocal spinning disk microscope. Actin appears in magenta and is stained using SiR Actin. A 2-µm wide Z-stack (three steps spaced by 1 µm) is acquired every 10 s and is then MAX projected onto a single plane. Playback speed: 5 frames per second.

Video 4.   **PtK2 cell expressing GFP tubulin 2 h after micro-injection with 1 µM of labelled tubulin (green) (**Fig. S2**).** Microtubules appear in red. Typical acquisition from which the kymographs in Fig. S2 A were built. The reader can visualize the interest of tubulin speckle microscopy in discriminating motion and dynamics along the lattice of the microtubules. Frames are acquired every 3 s over a 105-s period using a confocal spinning disk microscope. Playback speed: 5 frames per second.

Video 5.   **Control PtK2 cell stained using SIR-Actin (cyan), 2 h after micro-injection of 1 µM of labelled actin (magenta) (**Fig. S2**).** Typical acquisition from which the kymographs in Fig. S2 B were built. The reader can visualize contraction events along stress fibers with the presence of antiparallel speckle slidings along the length of the stress fibers. Frames are acquired every 1 min over a 30-min period using a confocal spinning disk microscope. Playback speed: 7 frames per second.

Video 6.   **Control PtK2 cell 2 h after its microinjection with both actin (magenta) and tubulin (green) (**Fig. 1**).** Representative responses of single microtubules in the 15 s that followed laser ablation. On the left, a microtubule depolymerization event after laser ablation with no mechanical relaxation. On the right, actin stress fiber recoiling after laser ablation accompanied by a local microtubule buckling and recoiling. Frames are acquired every 3 s over a 15 s period using a confocal spinning disk microscope. Playback speed: 3 frames per second.

Video 7.   **Control PtK2 cell 2 h after its microinjection with both actin (magenta) and tubulin (green) (**Fig. 1**).** Microtubule displacement event occurs when only actin was ablated. The white * on the video shows the localization of the laser impact inside the actin meshwork. Frames are acquired every 3 s over a 15-s period using a confocal spinning disk microscope. Playback speed: 3 frames per second.

Video 8.   **Repeated laser ablation experiment inside a PtK2 cytoplast expressing GFP tubulin treated with Jasplakinolide (600 nm) and Y27632 (20 µM) for 4 h (**Fig. 1**).** Microtubules appear in green. Microtubules are extensively and repeatedly depleted on one side of the centrosome during 5 min and the motion of the centrosome is recorded in parallel. A 2-µm wide Z-stack (three steps spaced by 1 µm) is acquired every 10 s using a confocal spinning disk microscope and is then MAX projected onto a single plane. Playback speed: 5 frames per second.

Video 9.   **Representative live centrosome recentering event showing the repositioning of the centrosome (gray) and the centroid (magenta) inside a PtK2 cytoplast expressing GFP tubulin (Nocodazole washout, Y27632 washout, and Cytochalasin D washout) (**Fig. 4**).** Microtubules appear in green. Nine selected time points are shown from a 4 h acquisition composed of 4-µm-wide Z-stacks (five steps spaced by 1 µm) acquired every 5 min using a confocal spinning disk microscope. The volume of the cytoplast is projected onto a single plane for all the time points. Images are processed following the described pipeline in the dedicated Materials and methods section. Playback speed: 3 frames per second.

Provided online is Table S1. Table S1 shows reagents and products.